A Two-Way Coupling Method for the Study of Aeroelastic Effects in Large Wind Turbines

Giacomo Della Posta[a,*], Stefano Leonardi[b], Matteo Bernardini[a]

[a] *Department of Aerospace and Mechanical Engineering, Sapienza University of Rome, Rome, RM, 00184, Italy*
[b] *Department of Mechanical Engineering, University of Texas at Dallas, Richardson, TX, 75080, USA*

Abstract

The relevant size of state-of-the-art wind turbines suggests a significant Fluid-Structure Interaction. Given the difficulties to measure the phenomena occurring, researchers advocate high-fidelity numerical models exploiting Computational Fluid and Structural Dynamics. This work presents a novel aeroelastic model for wind turbines combining our Large-Eddy Simulation fluid solver with a modal beam-like structural solver. A loose algorithm couples the Actuator Line Model, which represents the blades in the fluid domain, with the structural model, which represents the flexural and torsional deformations. For the NREL 5 MW wind turbine, we compare the results of three sets of simulations. Firstly, we consider one-way coupled simulations where only the fluid solver provides the structural one with the aerodynamic loads; then, we consider two-way coupled simulations where the structural feedback to the fluid solver is made of the bending deformation velocities only; finally, we add to the feedback the torsional deformation. The comparison suggests that one-way coupled simulations tend to overpredict the power production and the structural oscillations. The flapwise blades vibration induces a significant aerodynamic damping in the structural motion, while the nose-down torsion reduces the mean aerodynamic

*Corresponding author

Email addresses: giacomo.dellaposta@uniroma1.it (Giacomo Della Posta), stefano.leonardi@utdallas.edu (Stefano Leonardi), matteo.bernardini@uniroma1.it (Matteo Bernardini)

forces, and hence the power, yet without introducing a marked dynamical effect.

Keywords: Wind Energy, Aeroelasticity, Large-Eddy Simulation, Actuator Line Model, Modal Structural Dynamics, CFD-CSD method

2020 MSC: 74-10, 74F10, 76-10, 76F99

List of Symbols

$\boldsymbol{a_{rel}}$, $\boldsymbol{v_{rel}}$, $\boldsymbol{r_{rel}}$	Rel. body accel., vel. and position
$\boldsymbol{a}_s$	Abs. body acceleration
B	Number of the blades
C_P	Normalised Power
C_T	Normalised Thrust
C_l, C_d, C_m	Lift, drag and pitch.mom. coefficient
C_s	Smagorinsky model constant
$c, \bar{c}$	Local and average chord
D	Rotor diameter
$\mathbf{D}$	Modal struct. damp. matrix
$\mathbf{D}^{Co}$	Modal Coriolis damp. matrix
DEL	Damage Equivalent Load
d_i, θ_i	i-th transl. and rot. displ. component
$\boldsymbol{E}$	Body strain tensor
$\boldsymbol{E}_i$	i-th versor of $\mathcal{R}_E$
$\boldsymbol{E}_{\sigma_i}$	i-th versor of $\mathcal{R}_\sigma$
$\boldsymbol{e}^{Eu}$	Modal Euler loads vector
$\boldsymbol{e}$	Modal external loads vector
$\boldsymbol{e}^c$	Modal centrifugal loads vector
$\boldsymbol{e}_i$	i-th versor of $\mathcal{R}_e$
F	Prandtl correction factor
F_l, F_d, M^{aero}	Lift, drag and pitch. mom. per unit length
F^n, S^n, Φ^n	Fluid, struct. and load states at time n
FoR	Frame of Reference

F_2	Flapwise aerodyn. force per unit length
F_3	Edgewise aerodyn. force per unit length
$\boldsymbol{f_T}$	Resulting force on the structure
f	Frequency
$\boldsymbol{f^{aero}}$	Local aerodynamic force vector
$\boldsymbol{f}_s$, $\boldsymbol{t}_s$	Struct. ext. forces per unit vol. and surf.
$\boldsymbol{f^t}$	Turbine modelling body force vector
G	Body centre of mass
h	Hub height
$\boldsymbol{h}_G$	Angular momentum wrt centre of mass
I_d	Drivetrain rotational inertia
$\boldsymbol{J}_{g_i}$	Subvolume inertia tensor
$\boldsymbol{J}_{g_i}^{\delta}$	Subvolume inertia tensor minus half trace
$\mathbf{K}$	Modal stiffness matrix
$\mathbf{K}^{Eu}$	Modal Euler stiff. matrix
$\mathbf{K}^{c}$	Modal Centrif. stiff. matrix
k_{gen}	Torque gain
L	Blade length
M	Torsional aerodyn. mome. per unit length
M_i^R	Reaction mom. component around E_i
M_s	Number of modes
$\mathbf{M}$	Modal mass matrix
m_b	Blade mass
m_i	Subvolume mass
m_t	Body total mass
$\boldsymbol{m_{O'}}, \boldsymbol{m_G}$	Resulting mom. on the struct. wrt O' and G
N	Number of structural nodes
O, O'	Hub centre and blade root
$\boldsymbol{OP}$	Position vector wrt O
P	Power

P_r	Rotational frequency
PSD	Power Spectral Density
$\tilde{p}, \bar{p}$	Filtered and modified pressure
pdf	Probability density function
$\boldsymbol{q}$	Modal coordinate vector
R, R_h	Rotor and hub radii
Re	Reynolds number ($= U_\infty D/\nu$)
R_i	Reaction force component along E_i
$\boldsymbol{R_{OP}}$	Position vector wrt O in undef. config.
$\boldsymbol{R_{O'}}$	Undeformed position of O'
$\boldsymbol{R_{g_i}}$	Abs. position of $\mathcal{V}_i$ centre of mass
$\mathcal{R}_E$	FoR rotating with the blade
$\mathcal{R}_\Sigma$	Final Relative FoR
$\mathcal{R}_e$	Fixed Inertial FoR
R^Θ	Azimuthal change of basis matrix
R^ϕ	Pre-twist change of basis matrix
$\mathsf{R}^{e\to E}$	Matrix for change of basis $\mathcal{R}_e \to \mathcal{R}_E$
$\mathsf{R}^{e\to \Sigma}$	Matrix for change of basis $\mathcal{R}_e \to \mathcal{R}_\Sigma$
R^{el}	Angular def. change of basis matrix
$\boldsymbol{r}_{O'G}$	Centre of mass position in $\mathcal{R}_E$
$\boldsymbol{r_g}$	Rel. position wrt body centre of mass
r	Radial distance from the hub
r_η	Radial distance from actuator line
$\boldsymbol{r}$	Position vector wrt O'
$\tilde{S}_{ij}$	Filtered strain rate tensor
$\mathcal{S}, \mathcal{V}$	Body surf. and vol.
T	Thrust
T_{aero}	External aerodynamic torque
T_{gen}	Generator torque
TI	Turbulence Intensity

$\boldsymbol{T}_s$	Body stress tensor
t	Time
U_h	Hub height flow velocity
U_{rel}	Magnitude of rel. vel. in airfoil plane
U_∞	Undisturbed flow velocity ($= U_h$)
$\boldsymbol{u}^{\boldsymbol{P,abs}}$	Abs. fluid vel. at point P
$\boldsymbol{u}^{\boldsymbol{P,def}}, \boldsymbol{u}^{\boldsymbol{def}}$	Blade deformation vel.
$\boldsymbol{u}^{\boldsymbol{P,rel}}$	Rel. fluid vel. at point P
$\tilde{u}_i$	Filtered fluid vel.
$\mathcal{V}_i$	Body subvolume
$\boldsymbol{v}'$	Rel. vel. wrt centre of mass
$\boldsymbol{v}_G$	Centre of mass abs. vel.
v_i, ω_i	i-th comp. of transl. and rot. deform. vel.
X_i	i-th coordinate in $\mathcal{R}_E$
x_i or x, y, z	i-th coordinate in $\mathcal{R}_e$
$x_{i,c}$	cell-centre coordinate in i-th direction
$\boldsymbol{x}$	Body displacement
$\boldsymbol{x}_{O'}$, $\boldsymbol{a}_{O'}$	Blade root displ. and accel.

α	Local angle of attack
α_s	Shear exponent
Δ	Smagorinsky filter width
Δx_i	Grid spacing in i-th direction
ϵ	ALM spreading radius
ϕ	Pre-twist angle
ζ	Modal damping
$\boldsymbol{\zeta}$	Relative position in i-th subvol.
η	ALM kernel function
Θ	Azimuthal angle of ref. blade

λ	Tip speed ratio
ν	Kinematic air viscosity
ν_{sgs}	Subgrid eddy viscosity
ρ	Air density
ρ_s	Structure density
τ_{ij}	Sub-Grid Scale stress tensor
τ_{ij}^d	Deviatoric part of τ_{ij}
$\boldsymbol{\psi_m}$	m-th mode shape
$\boldsymbol{\psi^m}\|_{\boldsymbol{x}}$	m-th mode shape local displ. field
$\boldsymbol{\psi_t^m}\|_{\boldsymbol{g_i}}$, $\boldsymbol{\psi_r^m}\|_{\boldsymbol{g_i}}$	Displ. and rot. associated with m-th mode
$\boldsymbol{\Omega}$	Rotor angular velocity vector
ω_m, f_m	m-th angular and linear struct. eigenfreq.

$\mathcal{A}_n$	Skew-sym. tensor assoc. with Ψ_r^n
$\mathrm{sym}(\bullet)$	Symmetric part of a matrix
δ_{ij}	Kronecker delta
$\delta(\bullet)$	Virtual quantity
ϵ_{ijk}	Levi-Civita symbol
$\sigma_\bullet$	Standard deviation
$\cdot$	Scalar product
$\times$	Vector product
$\otimes$	Tensor product
$:$	Frobenius inner product
$(\bullet)^r$	Rated quantity
$(\dot{\bullet}), (\ddot{\bullet})$	First and second time derivatives
$\overline{\bullet}$	Time average
$\langle\bullet\rangle$	Phase average

1. Introduction

To reduce the cost of wind energy, the diameters of the wind turbines have been continuously increasing up to more than 200 m [1].

Even though scaling the turbines up ensures larger power production, such an extreme design also entails additional problems because of the new implicit requirements and constraints on the structure, and on the blades in particular. Nowadays, the blades of the Horizontal Axis Wind Turbines (HAWTs) are stiff enough to guarantee sufficient tower clearance and structural properties. Increasing dimensions and keeping stiffness constant would cause massive blades and expensive supports with huge nacelles and towers, which would result in impractical and inconvenient solutions. Thus, blades are going to be not only longer and slenderer, but also more flexible, and hence aeroelasticity will have to be considered during the design process to predict potential performance alterations and possible new instability problems affecting the turbine operating life [2].

Because of the complexity of the problem, analytical aeroelastic models have only limited applications; moreover, given the difficulties and the costs of controlled experiments and of field data gathering, only few extensive experimental studies of utility-scale turbines exist in literature [3]. For this reason, it is evident that numerical models of Fluid-Structure Interaction (FSI) play a fundamental role in the development of wind energy.

Nowadays, most numerical aeroelastic approaches describe the turbine aerodynamics by means of low-fidelity engineering models, in particular the widely used Blade Element Momentum (BEM) theory. For example, the standard multi-physics software OpenFAST [4], developed by the National Renewable Energy Laboratory (NREL) and formerly known as FAST, couples an aerodynamic module implementing BEM theory with a structural solver based on the Geometrically Exact Beam Theory (GEBT) [5], whose equations are discretised in space with Legendre spectral finite elements [6]. Similarly, the aeroelastic tool HAWC2 [7], developed by the Risø National Laboratory and the Technical

University of Denmark, couples the BEM aerodynamic model with a multi-body structural solver.

Despite its efficiency and effectiveness in a wide range of conditions, several studies [8, 9, 10, 11] have proved that BEM theory, even if corrected with engineering models [12], is unable to represent correctly the unsteady and multi-scale flow phenomena because of its strong limiting assumptions, which force designers to adopt conservative safety factors eventually undermining the competitiveness of wind turbines.

As a consequence, the wind energy community advocates the development of high-fidelity aeroelastic models that are able to study properly the effects of the unsteady fluid-structure-control interaction for the new big wind turbines [13]. As reported in the reviews of Hansen et al. [14] and Zhang and Shuhong [15], recent studies have tried to leverage the superior capabilities of Computational Fluid Dynamics (CFD) and Computational Structural Dynamics (CSD) with today's computational resources to describe accurately the fluid motion and the structural dynamics (CFD-CSD models).

In particular, the use of CFD provides high accuracy, also in off-design regimes, and allows researchers to gain a deeper physical insight in realistic turbulent conditions [16, 17]. However, because of the wide range of the spatial and temporal flow scales of the problem, Direct Numerical Simulation (DNS) of the Navier-Stokes equations is still beyond the reach even of today's supercomputers for Reynolds number typical of wind energy applications and in fluid domains including a fine resolution around the solid boundaries of the turbines. Turbulence modelling approaches based on the Reynolds Averaged Navier-Stokes (RANS) equations reduce the computational burden of the simulations, but are known to be not very accurate in the treatment of separated regions and of unsteady flows. The Large-Eddy Simulation (LES) approach, instead, allows researchers to model unsteady turbulent flows with superior accuracy compared to RANS, but with a minor computational expense compared to DNS. However, the necessary resolution to deal with wall-bounded flows increases the cost of the method, which tends to the one of the DNS method for high Reynolds numbers [18].

An alternative approach combining the benefits of CFD solvers and blade-element methods consists in the use of generalised actuator disc models [19]: the flow around the actual geometry of the blades is not resolved, but body forces act upon the incoming flow in the region that should be occupied by the blades, to mimic the action of the solid boundaries on the fluid motion. As a result, the 3D Navier-Stokes equations steer the dynamics of the wake under the action of the blades' aerodynamic loading, which instead is determined by means of a blade-element approach using the tabulated airfoil characteristics and the local flow kinematics. A popular example of such methods is the Actuator Line Model (ALM) [20], where the body forces are distributed along radial lines representing the blades and rotating with the angular rotor speed. In particular, this method has been proved effective in accurately reproducing wind turbines flow field especially in LES frameworks [21, 22, 23].

For what concerns the structural modelling, the main difficulties arise from the wind turbine blades, given their peculiar shapes and mechanical properties resulting from composite materials and given the high stiffness of the other components, such as the tower and the shaft. The structural dynamics models used in aeroelasticity are essentially the Finite Element Method (FEM), the multi-body formulation and the modal approach [14]. While FEM allows the description of complex deformation states, but with a potentially high computational expense, the modal approach offers a very cheap method to determine the structural response with satisfactory results. Finally, the multi-body formulation is a good compromise between the two methods above.

During the last years, several research groups have developed various high-fidelity CFD-CSD models, connecting different aerodynamics and structural formulations by means of different coupling procedures.

One of the first high-fidelity aeroelastic models was developed by Hsu and Bazilevs [24], which simulated the three-dimensional FSI of the complete NREL 5 MW reference onshore wind turbine [25], including the nacelle and the tower. The proposed method coupled tightly a low-order finite-element based ALE-

VMS technique for aerodynamics with a NURBS-based isogeometric structural analysis to study the rotor blades, modelled with thin composite shells. Kinematic and traction conditions were weakly imposed on a sliding interface. The simulations showed a strong impact of the tower on the torque and on the blade displacement, although the authors did not observe any relevant difference on the time-averaged power production from the comparison between rigid and flexible cases.

Other groups have tried to couple CSD models mostly with blade-resolved RANS fluid solvers. Heinz [26] coupled the structural multi-body formulation of HAWC2 [7] with the 3D RANS solver EllipSys3D [27], by means of a partitioned coupling method. The comparison of the strong and loose coupling implementations brought the authors to the conclusion that loose coupling methods are accurate enough for wind energy problems. Yu and Kwon [28] coupled an incompressible RANS solver employing mesh deformation techniques with a FEM beam solver by means of a loose coupling approach. For the same reference turbine studied by Hsu and Bazilevs, they confirmed the effect of tower interference on the structural dynamics. Moreover, they found that gravity essentially controlled the lead-lag bending in the plane of the rotor, and above all, that nose-down torsional deformation in the coupled simulations reduced relevantly the blade aerodynamic loads, and thus torque and thrust. The final results are in agreement with the behaviour observed also in other works using low-fidelity aerodynamic models [29, 30]. Dose et al. [31] simulated the same turbine of the previous cases, without the tower and the nacelle, by means of a loosely-coupled method joining the OpenFOAM 3D RANS solver [32], with dynamic mesh motion and deformation, and an in-house FEM solver based on GEBT [33]. The authors found a smaller torsional deformation of the blades compared to Yu and Kwon, and observed some differences between the rigid case and the deformable one only in yawed or tilted cases. Recently, Sprague et al. [34] presented ExaWind, an NREL open-source simulation environment for wind energy. This tool couples the Nalu-Wind CFD code [35], capable of using RANS, LES or even Detached-Eddy Simulation (DES) with or without actuator disc models, with the turbine-simulation code OpenFAST, by using a loose conventional serial-staggered algorithm [36]. First coupled blade-resolved RANS simulations for the NREL 5 MW turbine did not reveal a relevant effect of the deformation on the time-averaged wind turbine performance. The authors ascribed this effect to the stiff nature of the turbine's blades under study.

Li et al. [37] coupled a multi-body structural solver with a delayed DES fluid solver to analyse the behaviour of the NREL 5 MW turbine and considered a turbulent inflow generated by the Mann's model [38]. Information between the two independent solvers was exchanged at run-time, and dynamic overset grids solved grid deformations and relative motions of the wind turbine components. The results suggested that fluid quantities are rather insensitive to structural flexibility effects, and thus that, at the moment, wake analysis of multi-MW wind turbines can be performed under the assumption of rigid structure.

Other groups have tried to take advantage of the generalised actuator disc models in order to avoid generating blade-resolved meshes and to simplify the physical and computational interface between the fluid and the structural problems.

Storey et al. [39] coupled in a one-way approach the servo-elastic tool FAST [40] with the Actuator Sector Method [41] in their in-house LES solver. The FAST's Aerodyn package evaluated the aerodynamic forces along the blades from the local flow field. However, they still considered the turbine as rigid in the coupling procedure, and thus flexibility could not influence the determination of the local incidence of the blades. The NREL coupled the OpenFOAM LES fluid solver SOWFA (Simulator for Off/Onshore Wind Farm Applications) and its actuator line model with the engineering tool FAST, in which only flexural structural dynamics of the blades was considered by means of a modal method. Several works [42, 43] validated the aeroelastic tool and used it to appraise the effects of roughness and atmospheric stability on wind turbines, however without assessing extensively the isolated effect of the blades flexibility. Recently, Meng et al. [44, 45] coupled the actuator line model, first in RANS and then in LES framework, with a finite-difference structural solver for rotating Euler-Bernoulli beams. The structural solver accounted only for in- and out-of-the-plane bending, and the two-way coupling procedure included in the definition of the local effective angle of attack only the additional effect of the structural vibration velocities. The simulations neglected the effect of the tower and the nacelle, and the analysis was mainly concerned on structural issues.

The aim of this work is to propose a novel two-way coupling high-fidelity CFD-CDS model for the study of the aeroelasticity for wind turbines. The method couples our in-house LES solver with a modal beam-like solver, by means of a loose staggered coupling algorithm. Thus, we are able to both describe fluid phenomena with high accuracy and simultaneously represent, in an efficient way, the structural dynamics of the cantilever blades clamped at the hub. The method takes advantage of the Actuator Line Model formulation and uses it as a natural and efficient interface between the fluid and the structural subproblems to mutually exchange information about the blades loading and motion. In particular, the blade dynamics can include also the instantaneous torsional Degree of Freedom (DF) and the complete elastic state in general, which is a novelty among the aeroelastic solvers based on the generalised actuator disc models in LES framework, to the authors' knowledge. Moreover, because of their crucial role in the problem, the model includes in the fluid domain also the tower and the nacelle, assumed to be rigid, by means of an Immersed Boundary Method (IBM) [46].

We carried out three separate sets of simulations, and we compared their results. In the first case, named "ALM" case, we considered turbulent simulations with one-way coupling, in which only the fluid solver provided at run-time the structural solver with the aerodynamic loads. Then, we carried out two-way coupled simulations using two different structural feedbacks to the fluid solver: in the first case, named "ALM/IV" case, we considered a structural feedback made only of the instantaneous bending deformation velocities of the blades; in the second case, named "ALM/IVT" case, we included in the definition of the incidence also the instantaneous torsional deformation of the blades.

Given the fact that its features and mechanical properties are well-documented and its behaviour has been widely studied in literature [24]-[45], here we consider the NREL 5 MW onshore baseline wind turbine.

This paper is organised as follows. In Section 2 we present the methodology used for the fluid and the structural subproblems, and we describe how we coupled them. In Section 3, we report the physical and numerical setup taken into consideration, and we outline the cases treated, and then in Section 4 we present the results of the numerical simulations. Finally, in Section 5 we comment our main findings, and we outline possible future developments of our work.

2. Methodology

In the following sections, we present the methodology adopted to simulate the aeroelastic interaction for a stand-alone wind turbine in a fully-turbulent flow. In Section 2.1 we describe our fluid solver and rotor modelling, in Section 2.2 we illustrate the structural model for the cantilever blades, and finally in Section 2.3 we characterize the aeroelastic coupling procedure.

2.1. The fluid model

Our in-house UTD-WF code [47] carries out Large-Eddy Simulations under the assumption of incompressibile flow. Denoting with indices the vector or tensor components along the x_i axes defining the fixed Frame of Reference (FOR) $\mathcal{R}_e$ (see Figure 1) and adopting the Einstein notation, the filtered governing equations are:

$$\frac{\partial \tilde{u}_i}{\partial x_i} = 0\,, \tag{1}$$

$$\frac{\partial \tilde{u}_i}{\partial t} + \frac{\partial \tilde{u}_i \tilde{u}_j}{\partial x_j} = -\frac{\partial \bar{p}}{\partial x_i} + \frac{1}{Re}\frac{\partial \tilde{u}_i}{\partial x_j \partial x_i} - \frac{\partial \tau_{ij}^d}{\partial x_j} + f_i^t\,, \tag{2}$$

where $\tilde{u}_i$ are the filtered velocity components; $\bar{p}$ is the modified pressure, which is the sum of the filtered pressure $\tilde{p}$ and the isotropic part of the Sub-Grid Scale (SGS) tensor $\tau_{ij} = \widetilde{u_i u_j} - \tilde{u}_i \tilde{u}_j = \tau_{ij}^d + \frac{1}{3}\tau_{kk}\delta_{ij}$; Re is the Reynolds number based on the turbine's diameter D, the undisturbed inflow velocity U_∞ and

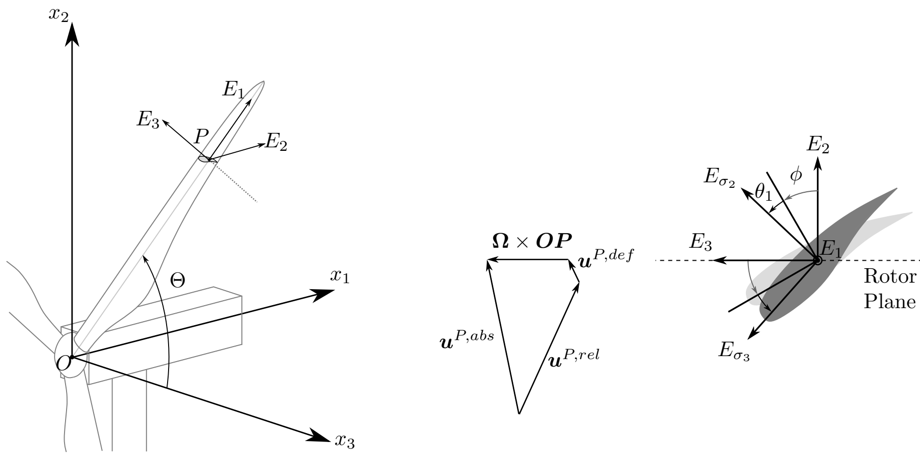

Figure 1: Different Frames of Reference defined for the description of the FSI problem of wind energy. The frame $\mathcal{R}_E$ rotates rigidly around the hub centre O and is identified by the azimuthal angle Θ of each blade, with E_2 constantly pointing at the positive streamwise direction. In correspondence of a generic section at point P along the blade, the blade pre-twist ϕ and the instantaneous angular deformation (only torsion is shown in figure) define the local Frame of Reference $\mathcal{R}_\Sigma$, where the effective angle of attack is defined. The velocity vectors show the combination of the different components in the plane of a generic profile.

the kinematic viscosity of the air ν; f_i^t are the components of the body forces introduced by the turbine modelling (see Section 2.1.1). The Smagorinsky SGS model [48] expresses the deviatoric part of the residual stress tensor under the Boussinesq's hypothesis:

$$\tau_{ij}^d = -\nu_{sgs}\left(\frac{\partial \tilde{u}_i}{\partial x_j} + \frac{\partial \tilde{u}_j}{\partial x_i}\right) = -2\nu_{sgs}\tilde{S}_{ij} = -2\left[(C_s\Delta)^2\sqrt{2\tilde{S}_{ij}\tilde{S}_{ij}}\right]\tilde{S}_{ij}\,, \tag{3}$$

where ν_{sgs} is the subgrid eddy viscosity, $\tilde{S}_{ij}$ is the filtered strain rate tensor, C_s is the model constant and $\Delta = (\Delta x_1 \Delta x_2 \Delta x_3)^{1/3}$ is the (implicit) filter width defined by the grid spacings Δx_i in the three fixed directions. According to previous works [49, 50], we tuned the model constant C_s to the value of 0.09 for wind energy simulations.

Eqs. 1 - 2 are discretised by means of the finite difference method on an orthogonal staggered grid, to avoid odd-even decoupling between pressure and velocity. Energy-conserving central schemes approximate derivatives in space with second-order accuracy. A fractional-step method integrates equations in time by means of a hybrid third-order low-storage Runge-Kutta (RK) scheme that treats implicitly viscous linear terms and explicitly convective nonlinear terms. The interested reader can refer to Orlandi [51] for more details on the adopted numerical scheme.

The code is written in Fortran, is parallel, and uses the Message Passing Interface (MPI) paradigm.

2.1.1. Rotor modelling in the fluid domain

The rotor inside the fluid domain is modelled according to the ALM proposed by Sorensen and Shen [20]: the aerodynamic forces are determined by means of a blade-element approach and are then distributed as body forces along rotating lines in correspondence of the position of the blades.

According to the blade element theory, for a 2D airfoil located at distance r from the hub centre, the lift force F_l and the drag force F_d per unit length are

$$F_l = \frac{1}{2}\rho U_{rel}^2 c\, C_l(\alpha) F \qquad \text{and} \qquad F_d = \frac{1}{2}\rho U_{rel}^2 c\, C_d(\alpha) F\,, \tag{4}$$

where ρ is the air density, U_{rel} is the magnitude of the local relative velocity in the plane of the airfoil, c is the local chord length of the airfoil, $C_l(\alpha)$ and $C_d(\alpha)$ are the lift and drag coefficients for a certain local angle of attack α, and F is a modified Prandtl correction factor.

The look-up tables of the aerodynamic coefficients of 2D airfoils neglect three-dimensional effects, and therefore, to correct the typical overprediction of the loads at the blade tip and root, we use in Eqs. 4 a modified Prandtl tip correction factor [52] given by:

$$F = \frac{4}{\pi^2}\cos^{-1}\left[\exp\left(-g\frac{B}{2}\frac{R-r}{r\sin(\alpha+\phi)}\right)\right]\cos^{-1}\left[\exp\left(-g\frac{B}{2}\frac{r-R_h}{r\sin(\alpha+\phi)}\right)\right],$$
$$\text{with} \quad g = \exp\left[-0.125\,(B\,\lambda - 21.0)\right] + 0.1\,, \tag{5}$$

where B is the number of the blades, R is the radius of the rotor, R_h is the hub radius, ϕ is the local twist angle of the blade, $\lambda = \Omega R/U_\infty$ is the tip speed ratio, and Ω is the rotor angular speed.

The total *local* aerodynamic force vector $\boldsymbol{f}^{aero}$, made of lift and drag, is then projected onto the flow. A 2D Gaussian kernel spreads the aerodynamic forces in cylinders surrounding each actuator line, to avoid numerical instabilities arising from eventual concentrated forces in the fluid domain. Thus, in Eq. 2, the body force vector $\boldsymbol{f}^t$ acting on the fluid in the cylindrical regions of the actuator lines is equal to

$$\boldsymbol{f}^t = -\boldsymbol{f}^{aero}\eta = -\boldsymbol{f}^{aero}\frac{1}{\epsilon^2\pi}\exp\left[-\left(\frac{r_\eta}{\epsilon}\right)^2\right] , \tag{6}$$

where r_η is the radial distance of a generic point of the cylinder from the relative actuator line and ϵ is the spreading parameter. Several studies have shown that the spreading parameter ϵ strongly influences the evolution of the flow field and its most appropriate value is still debated. Troldborg et al. [53] suggested a dependence of the spreading parameter on the grid spacing, and specifically that it should be such that $\epsilon/\Delta \geq 2$ to avoid numerical instabilities. On the other hand, recent studies [54, 55] have proposed to link ϵ to the distribution of the chord length. In particular, Martínez-Tossas et al. [56] concluded that for simulations with grid spacing larger than the chord, ϵ should be a function of Δ, whereas for grid spacing smaller than the chord, ϵ should be a function of c. To avoid unfeasible grid requirements for our computational resources, a spreading radius $\epsilon = 2\,\Delta$ is used for our simulations, corresponding to $\epsilon/\bar{c} = 0.85$, where $\bar{c}$ is the average chord of the blade.

Finally, to estimate the aerodynamic pitching moment acting on the blades with respect to the structural pitching axis passing through the quarter of chord, we follow similarly a blade-element approach. Thus, the pitching moment per unit length referred to the airfoil quarter of chord is equal to

$$M^{aero} = -\frac{1}{2}\rho U_{rel}^2 c^2 C_m(\alpha) F \, , \tag{7}$$

where $C_m(\alpha)$ is the local pitching moment coefficient. The minus sign takes into account that, by convention, the aerodynamic moment coefficient is positive when it pitches the airfoil in the nose-up direction, and thus induces a negative rotation around the positive structural pitching direction defined by E_1 in Figure 1 (see Section 2.2).

Finally, the tower and the nacelle are modelled by means of the IBM procedure validated in Santoni et al. [57], and the low-shaft angular speed Ω is evaluated from the single-DF model equation balancing the external aerodynamic torque T_{aero} and the generator torque T_{gen}:

$$I_d \, \dot{\Omega} = T_{aero} - T_{gen} \,, \tag{8}$$

where I_d is the drivetrain rotational inertia, which includes the combined inertia of the rotor and of the generator. We consider a variable-speed turbine operating in region II, for which the standard quadratic control law [58] holds and is such that:

$$T_{gen} = k_{gen} \Omega^2 \,, \tag{9}$$

where the torque gain k_{gen} is a function of the optimal tip speed ratio of the turbine, which for the NREL 5 MW turbine is $\lambda_{opt} \approx 7.5$.

2.2. The structural model

In a wind turbine, the rotor blades are the most flexible components and the most important parts from the aerodynamic point of view. Several studies have shown that their modal properties strongly affect the dynamics of the complete structure [59], and that the analysis of the isolated blades is also sufficient to estimate correctly aeroelastic properties of the entire structure, such as the flutter speed [2]. Moreover, the tower and the shaft are rather stiff and their deflections are usually small.

Because of this, we consider in our aeroelastic model only the structure of the blades. In particular, the blades are modelled as rotating beams rigidly clamped at the hub (cantilever beams), under the assumption of small deformations with respect to a relative FOR $\mathcal{R}_E$ (see Figure 1). We indicate with E_1 the direction of the pitching axis, coincident with the neutral axis of the blade passing through the quarter of chord [25], with E_2 the out-of-plane flapwise direction pointing at the positive streamwise direction, and with E_3 the in-plane edgewise direction, so that the FOR $\mathcal{R}_E$ has a right-handed coordinate system.

Under the assumption of linearity, the elastic generalised displacement $\boldsymbol{d}$, including translational d_i and rotational θ_i DFs, is thus decomposed along the coordinate X_1 on the neutral axis as

$$\boldsymbol{d}\left(X_1, t\right) = \sum_{m=1}^{M_s} q_m(t)\, \boldsymbol{\psi}^m\left(X_1\right) \tag{10}$$

where $\boldsymbol{\psi}^m\left(X_1\right)$ is the m-th elastic mode shape from the modal analysis of the structure, q_m is the corresponding modal coordinate and M_s is the number of modes used.

The general inertial coupling is included in modal basis by means of the methodology introduced by Reschke [60]. Given the difference of our case, we removed the assumption of mean axes, *i.e.* origin of the structural coordinate system at the instantaneous centre of mass, and we derived the inertial coupling terms for a generic origin. In our case, the origin is fixed at the rotor centre O.

Firstly, we derived the rigid-body (translation and rotation) and elastic equations by means of the virtual work principle. We assumed a generic virtual displacement made of rigid and elastic virtual motion, and we considered the decomposition of the acceleration of the body in the moving FOR $\mathcal{R}_E$ rigidly rotating with each blade. Thus, we obtained a formulation accounting for the two-way coupling between rigid-body and structural dynamics. However, we neglected the rigid-body equations because we are not interested in the rigid translation of the rotor, and we assume a fixed inertia in Eq. 8, without considering any modification of the rotor inertia caused by the deformation of the blades. The remaining equations were a system of elastic equations where the angular velocity and acceleration of the structural FOR $\mathcal{R}_E$ were independently evaluated in Eq. 8 (one-way rigid-body coupling). Hence, we obtained that

$$\mathbf{M}\,\ddot{\boldsymbol{q}} + \left[\mathbf{D} + \mathbf{D}^{Co}\left(\boldsymbol{\Omega}\right)\right]\dot{\boldsymbol{q}} + \left[\mathbf{K} + \mathbf{K}^{c}\left(\boldsymbol{\Omega}\right) + \mathbf{K}^{Eu}(\dot{\boldsymbol{\Omega}})\right]\boldsymbol{q} = \boldsymbol{e} + \boldsymbol{e}^{c}\left(\boldsymbol{\Omega}\right) + \boldsymbol{e}^{Eu}(\dot{\boldsymbol{\Omega}}) \tag{11}$$

where $\mathbf{M}$ and $\mathbf{K}$ represent the modal structural mass and stiffness matrices respectively, and $\boldsymbol{e}$ are the external loads in modal basis, which include the gravity force acting on the local centre of mass and the ALM aerodynamic forces acting on the local quarter of chord. Given the assumption of linearity, we apply all the forces to the reference undeformed configuration. The elastic mode shapes are normalised to unit mass, such that $\mathrm{M}_{nm} = \delta_{mn}$ and $\mathrm{K}_{nm} = \omega_n^2 \delta_{mn}$, where ω_n is the n-th natural angular eigenfrequency and $n, m = 1, \ldots, M_s$. A constant modal damping ζ is assumed, such that the structural damping matrix is $\mathrm{D}_{mn} = 2\zeta\omega_n\delta_{mn}$. We indicate time derivation of structural quantities and angular speed with $(\dot{\bullet})$.

We include the effects of the centrifugal acceleration in the terms

$$\mathrm{K}^c_{nm} = -\boldsymbol{\Omega} \cdot \mathrm{sym} \left\{ \iiint_{\mathcal{V}} \rho_s \left[\left(\boldsymbol{\psi}^m \cdot \boldsymbol{\psi}^n \right) \mathbf{I} - \boldsymbol{\psi}^m \otimes \boldsymbol{\psi}^n \right] \mathrm{dV} \right\} \boldsymbol{\Omega} \,, \tag{12}$$

$$\mathrm{e}^c_n = \boldsymbol{\Omega} \cdot \mathrm{sym} \left\{ \iiint_{\mathcal{V}} \rho_s \left[\left(\boldsymbol{R}_{OP} \cdot \boldsymbol{\psi}^n \right) \mathbf{I} - \boldsymbol{R}_{OP} \otimes \boldsymbol{\psi}^n \right] \mathrm{dV} \right\} \boldsymbol{\Omega} \,, \tag{13}$$

the effects of the Coriolis acceleration in the term

$$\mathrm{D}^{Co}_{nm} = 2\,\boldsymbol{\Omega} \cdot \iiint_{\mathcal{V}} \rho_s \left(\boldsymbol{\psi}^m \times \boldsymbol{\psi}^n \right) \mathrm{dV} \,, \tag{14}$$

and the effects of the Euler acceleration in the terms

$$\mathrm{K}^{Eu}_{nm} = \dot{\boldsymbol{\Omega}} \cdot \iiint_{\mathcal{V}} \rho_s \left(\boldsymbol{\psi}^m \times \boldsymbol{\psi}^n \right) \mathrm{dV} \,, \tag{15}$$

$$\mathrm{e}^{Eu}_n = -\dot{\boldsymbol{\Omega}} \cdot \iiint_{\mathcal{V}} \rho_s \left(\boldsymbol{R}_{OP} \times \boldsymbol{\psi}^n \right) \mathrm{dV} \,, \tag{16}$$

where $\otimes$ indicates the tensor product operation, $\boldsymbol{R}_{OP}$ is a vector connecting the origin to the generic point P in the undeformed configuration, $\mathbf{I}$ is the identity matrix, sym indicates the symmetric part of a matrix, ρ_s is the structural density, and $\mathcal{V}$ is the volume occupied by the structure.

The inertial terms are discretised by means of the method presented in Saltari

Table 1: A comparison with other results in literature of the first six natural frequencies f_m for the stand-alone blades of the NREL 5 MW wind turbine with the main features of the corresponding eigenmodes.

Freq.	Present [Hz]	BMODES [Hz]	FAST [Hz]	Jeong et al. [29] [Hz]	Mode
f_1	0.68	0.69	0.68	0.67	1st flapwise
f_2	1.09	1.12	1.10	1.11	1st edgewise
f_3	1.95	2.00	1.94	1.93	2nd flapwise
f_4	4.00	4.12	4.00	3.96	2nd edgewise
f_5	4.52	4.64	4.43	4.43	3rd flapwise
f_6	5.58	5.61	5.77	5.51	1st torsional

et al. [61]. In particular, we express the above global volume integrals as a summation of volume integrals on each element of a FEM model of the structure, while we approximate locally the continuous mode shapes by means of a rigid motion defined by the discrete mode shapes from the modal analysis. We thus express Eqs. 12-16 only in terms of information known from the FEM model of the structure and from the mode shapes obtained from modal analysis.
For the detailed derivation and discretisation of the inertial coupling terms see the Appendix A.

For the modal analysis, we use a finite element model of the blade based on complete beam elements with 6 DFs, with Euler-Bernoulli behaviour for bending in directions E_2 and E_3, and linear shape functions for axial and torsional deformations [62]. We assume a lumped-mass representation, and we take into account the local offset of the centres of mass with respect to E_1 by means of the formulation in Reschke [60]. Finally, the structural matrices are assembled considering the local twist.
Table 1 reports the first natural frequencies of the isolated blade of the reference turbine. These are in good agreement with the frequencies of the complete structure indicated in the reference technical report and in other studies [25, 29, 31].

The generalised-α method [63] advances the structural dynamics in time. This one-step three-stage time integration method is unconditionally stable for linear problems, second-order accurate, self-starting, and has a controllable algorithmic dissipation. Moreover, it has an optimal combination of high dissipation of the high-frequency modes and low dissipation of the low-frequency modes.

2.3. The aeroelastic coupling approach

Usually, the ALM assumes a rigid motion of the actuator lines and estimates the effective angle of attack only from the fluid velocity sampled at the position of the lines and from the rotational velocity at each section.

In our two-way coupling aeroelastic model, we link the ALM with the described structural approach as shown in Figure 2. The model is based on two independent or partitioned solvers that exchange information once per time step (loose partitioned coupling approach) [26]. At the beginning of each RK time substep n, the distribution of the effective angle of attack α^n is estimated along each blade from the fluid state F^n (consisting of the velocity field), the angular speed Ω^n, and the elastic state S^n. In particular, the elastic state can include only the deformation velocity $\boldsymbol{u}^{def}$ or also the local vector of the deformation angles $\boldsymbol{\theta}$, which determines the instantaneous orientation of each section. Given the look-up tables of the aerodynamic coefficients of the airfoils, the distributions of the aerodynamic forces and moments per unit length Φ^n, used in the ALM, are evaluated by means of a blade element approach. In order to determine the structural state at the following instant S^{n+1}, the aerodynamic forces are assumed to remain constant inside each RK substep, and thus the external loading at time $n+1$, required by the generalised-α method, is approximated by Φ^n.

We implemented, therefore, a Non-Conventional Serial-Staggered (NCSS) algorithm [36], given the fact that we did not correct exactly the prediction of the structural deformation after the final evaluation of the fluid state, but instead we limited inter-field communications only at the beginning of each RK substep, and we used the consecutive approximations of the aerodynamic forces available at those instants. This allows us to leverage the knowledge of the aerodynamic loading from the RK scheme of the fluid solver to increase the accuracy of the structural scheme, without re-evaluating the forces and the structural state in

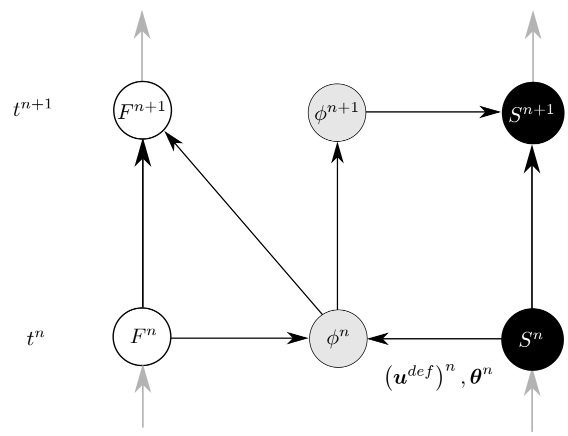

Figure 2: Ladder-like scheme of the two-way coupling method for RK-steps n and $n+1$. The fluid state F is indicated on the left, the structural state S is indicated on the right. The aerodynamic loading Φ and its estimations are indicated in the middle; $\boldsymbol{u}^{def}$ is the local deformation velocity, and $\boldsymbol{\theta}$ is the local vector of the deformation angles.

correspondence of the new fluid state, and thus preserving the overall efficiency of the code.

Because of the presence of different FORs, we define the relative velocity and the effective angle of attack in Eqs. 4 and Eq. 7 by means of a matricial notation. To describe the model, we adopt in this section the convention according to which (see Figure 1):

- the lower-case subscript indices refer to the components in the inertial FOR $\mathcal{R}_e$;
- the upper-case subscript indices refer to the components in the FOR $\mathcal{R}_E$ rigidly rotating with each blade;
- the lower-case greek subscript indices refer to the components in the local FOR $\mathcal{R}_\Sigma$, defined by the instantaneous orientation of each section.

According to the method presented, we express the relative velocity $\boldsymbol{u}^{P,rel}$ of a point P belonging to an actuator line as

$$\boldsymbol{u}^{P,rel} = \boldsymbol{u}^{P,abs} - \boldsymbol{u}^{P,def} - \boldsymbol{\Omega} \times \boldsymbol{OP}\,, \tag{17}$$

where $\boldsymbol{u}^{P,abs}$ is the value sampled at point P of the absolute fluid velocity, $\boldsymbol{u}^{P,def}$ is the deformation velocity of the blades described by the modal composition of $\dot{\boldsymbol{q}}$, and $\boldsymbol{\Omega} \times \boldsymbol{OP}$ is the rotational velocity. To determine the local flow at each section, assuming null yaw error, we express the relative velocity in $\mathcal{R}_\Sigma$ in Einstein notation as follows,

$$u_\sigma^{P,rel} = \mathsf{R}_{\sigma j}^{e\to\Sigma}\, u_j^{P,abs} - \mathsf{R}_{\sigma J}^{E\to\Sigma}\, u_J^{P,def} - \mathsf{R}_{\sigma j}^{e\to\Sigma}\, \epsilon_{jkm}\Omega_k OP_m. \tag{18}$$

where $\mathsf{R}_{\sigma j}^{e\to\Sigma}$ and $\mathsf{R}_{\sigma J}^{E\to\Sigma}$ are the matrices that define, respectively, the change from the basis of $\mathcal{R}_e$ to the basis of $\mathcal{R}_\Sigma$ and from the basis of $\mathcal{R}_E$ to the basis of $\mathcal{R}_\Sigma$. The matrix $\mathsf{R}_{\sigma J}^{E\to\Sigma}$ is given by the ordered composition of the matrix R^ϕ, describing the change of coordinates determined by the local blade twist ϕ around the pitch axis, and the matrix R^{el}, describing the change of coordinates determined by the local angular deformations that define the airfoil planes. These last angles are referred to the structural reference configuration $\mathcal{R}_E$ of each blade and are evaluated from the structural dynamics. By convention, the angle θ_i around direction $\boldsymbol{E}_i$ is positive according to the right-hand rule, and the rotation in space of the airfoil planes is determined by the sequence of finite rotations $\theta_1 \to \theta_2 \to \theta_3$ under the assumption of small angular deformations. Finally, the matrix $\mathsf{R}_{\sigma j}^{e\to\Sigma}$ includes also the azimuthal rotation of each blade Θ, described by the matrix R^Θ.

By assuming that for $\Theta = 0$ rad the generic blade is along the x_3 positive direction, it follows that

$$\begin{gathered}\mathsf{R}^{e\to\Sigma} = \mathsf{R}^{E\to\Sigma}\,\mathsf{R}^\Theta = \left(\mathsf{R}^\phi\,\mathsf{R}^{el}\right)\,\mathsf{R}^\Theta = \\ = \begin{bmatrix} 1 & 0 & 0 \\ 0 & \cos\phi & \sin\phi \\ 0 & -\sin\phi & \cos\phi \end{bmatrix} \begin{bmatrix} 1 & \theta_3 & -\theta_2 \\ -\theta_3 & 1 & \theta_1 \\ \theta_2 & -\theta_1 & 1 \end{bmatrix} \begin{bmatrix} 0 & \sin\Theta & \cos\Theta \\ 1 & 0 & 0 \\ 0 & \cos\Theta & -\sin\Theta \end{bmatrix}\end{gathered} \tag{19}$$

In accordance with the definition of the reference directions of $\mathcal{R}_\Sigma$, we express the effective angle of attack and the relative velocity in Eqs. 4 for the generic

Table 2: Parameters of the reference turbine.

Parameter	Symbol	Value	Units
Rated power	P^r	5	MW
Rated wind speed	U_∞^r	11.4	m/s
Rated angular speed	Ω^r	1.27	rad/s
Rotor diameter	D	126.0	m
Blade length	L	61.5	m
Hub height	h	90.0	m
Blade mass	m_b	17740	kg

point P on the actuator line as

$$\alpha = \mathrm{atan}\left(-\frac{u_{\sigma_2}^{P,rel}}{u_{\sigma_3}^{P,rel}}\right) \quad \text{and} \quad U_{ref} = \sqrt{\left(u_{\sigma_2}^{P,rel}\right)^2 + \left(u_{\sigma_3}^{P,rel}\right)^2}, \tag{20}$$

where we consider only the components in the plane of the local profile on directions σ_2 and σ_3.

By means of the described model, we are able to consider the effects of various levels of complexity in the coupling configuration. In the two-way coupled simulations of this work, we consider in the ALM/IV case the effects on the incidence of the flap- and edgewise deformation velocities without any angular deformation ($u_J^{P,def} \neq 0$ in Eq. 18 and $\theta_1 = \theta_2 = \theta_3 = 0$ in Eq. 19), while we include in the ALM/IVT case also the first-order effect of the torsional angle θ_1 ($u_J^{P,def} \neq 0$ in Eq. 18 and $\theta_1 \neq 0$, $\theta_2 = \theta_3 = 0$ in Eq. 19).

3. Geometrical and numerical setup

The stand-alone turbine considered in this work is the NREL 5 MW baseline wind turbine [25], which has a rotor diameter of $D = 126\,\mathrm{m}$ and three composite blades of length $L = 61.5\,\mathrm{m}$. Table 2 reports a brief summary of the features of the turbine.

The fluid computational domain considered (Figure 3) is equal to $9.0\,\mathrm{D} \times 10.0\,\mathrm{D} \times 2.88\,\mathrm{D}$ in the streamwise, wall-normal and spanwise inertial directions respec-

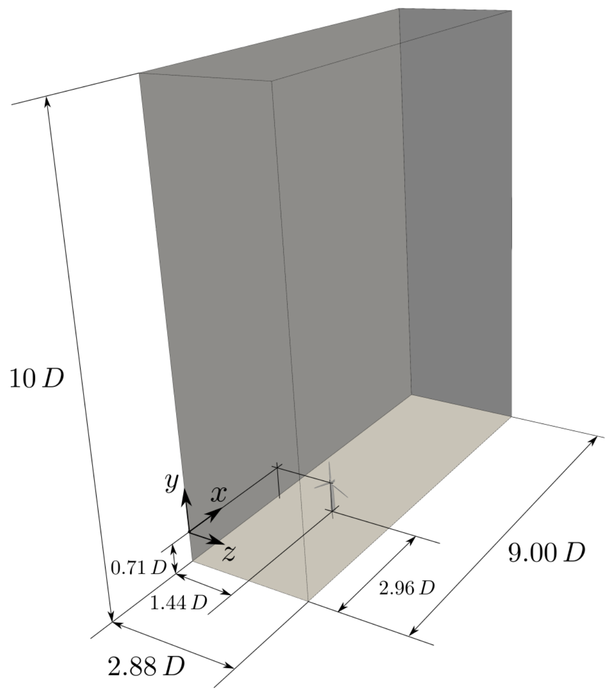

Figure 3: Fluid computational domain.

tively. The domain is discretised by means of an orthogonal mesh of $1296 \times 432 \times 432$ points, equally distributed in the streamwise and spanwise direction. A uniform vertical spacing is used in the lowest part of the domain (first $2\,D$), such as to obtain an isotropic grid in the region occupied by the wind turbine, and then the grid is stretched in wall-normal direction to limit the grid requirements of the simulations. Figure 4 shows the cell spacing in the vertical direction. The number of points per rotor diameter for the ALM model is 150. A grid sensitivity study, not shown here for brevity, confirmed the results reported in Section 4, for grids with 50 and 200 points per diameter. The hub of the turbine is located at the spanwise centre, *i.e.* $z/D = 1.44$, and at a streamwise distance from the inlet equal to $x/D = 2.96$.

Given the fact that turbulence and flow asymmetries caused by wind shear can be sources of unsteadiness for the blade dynamics, we assume to operate in a sheared turbulent condition. Hence, inflow turbulent fluctuations are de-

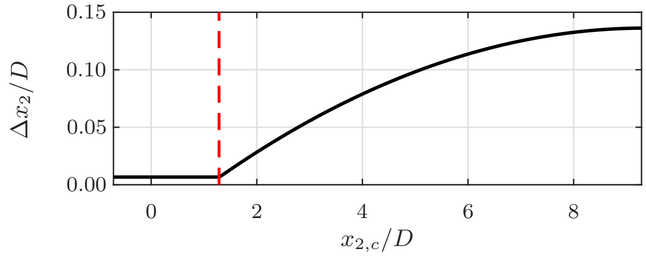

Figure 4: Vertical grid distribution. Cell spacing $\Delta x_2/D$ as a function of the corresponding nondimensional cell centre coordinate $x_{2,c}/D$. The dashed line in red indicates the end of the uniform grid region. More than the half of the points is concentrated in the proximity of the rotor.

rived from a precursor simulation in a fully periodic domain with cubic surface roughness, and are superimposed on a mean streamwise velocity profile defined by a power law with shear exponent equal to $\alpha_s = 0.14$ and mean hub velocity equal to $U_h = 10\,\mathrm{m/s}$. Turbulence intensity at the hub height is $TI = 2\%$. We prescribe periodic boundary conditions at the lateral boundaries of the computational box, free-slip boundary condition at the top surface, and radiative boundary conditions at the outlet. A Van Driest damping function [64] is used to correct the behaviour of the flow in the proximity of the no-slip bottom wall.

To describe the structural dynamics of the blades, we carried out at first a sensitivity study, which we do not report here for brevity, to decide the proper number of modes and structural nodes for the problem. We finally chose a number of modes $M_s = 15$ and a structural discretisation of the blades given by $N = 80$ equally-spaced nodes. Because of the different number and position of the aerodynamic points along the actuator line and the structural nodes of the blades, we deduce the quantities of mutual interest (forces and blade motion) by means of a polynomial interpolation that, in the case of the aerodynamic loading, take care of preserving the global resulting force.

We ran each of the three simulations sets (ALM, ALM/IV and ALM/IVT) at a Reynolds number $Re = 8.5 \times 10^7$ for approximately 60 revolutions, corresponding to almost $300\,s$, after the initial transient.

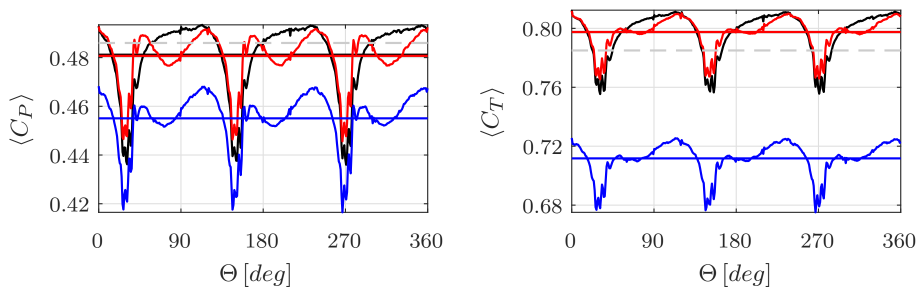

(a) C_P (b) C_T

Figure 5: Phase average of the power and thrust coefficients. ALM —, ALM/IV —, ALM/IVT —, BEM [25] - -. Horizontal straight lines indicate the corresponding time-averaged values.

4. Results

In this section, we present the results obtained from the comparison of the three sets of simulations carried out. First, we analyse the behaviour of the power and thrust coefficients, then we discuss the structural dynamics in terms of displacement and deformation velocity. Next, we consider the change of the aerodynamic forces and the dynamics of the root reaction. Finally, we present a fluid analysis presenting mean field slices and visualisations of the coherent structures in the domain.

4.1. Power and thrust coefficients

From the time history of the power coefficient C_P and the thrust coefficient C_T, normalised by means of the mean hub velocity U_h, we computed the phase-averaged behaviour reported in Figure 5, to filter out the instantaneous fluctuations due to the turbulent inflow. Hereinafter, we indicate the time average with an overbar symbol $\overline{\bullet}$ and the phase average with angle brackets $\langle \bullet \rangle$. The periodic passage of the blades in front of the tower induces a tower shadow effect with a drop in the power and thust coefficients by about 10 %. The blade vibration influences the aerodynamic forces especially when the blade passes in front of the tower, consistently with previous observations [37]. In particular, the addition of the aeroelastic coupling reduces the amplitude of the oscillations, and thus the standard deviation of the two coefficients (Table 3).

Table 3: Comparison of the statistics of the power and thrust coefficients between the cases considered. The last two columns report the percentage difference of the statistics for the ALM/IV and ALM/IVT cases with respect to the ALM one.

	BEM	ALM	ALM/IV	ALM/IVT	$\Delta_{ALM/IV}$	$\Delta_{ALM/IVT}$
$\overline{C}_P$	0.4860	0.4812	0.4807	0.4551	- 0.1 %	- 5.4 %
$\overline{C}_T$	0.7860	0.7975	0.7975	0.7117	0.0 %	- 10.8 %
σ_{C_P}	–	0.0167	0.0128	0.0133	- 23.3 %	- 20.4 %
σ_{C_T}	–	0.0165	0.0130	0.0133	- 21.2 %	- 19.4 %

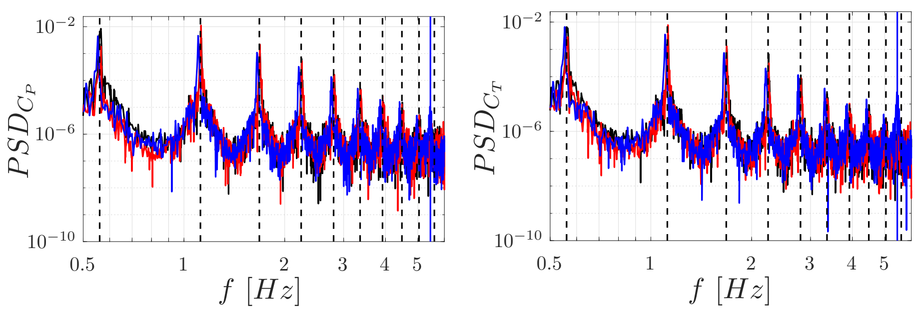

(a) C_P

(b) C_T

Figure 6: Power Spectral Density (PSD) of the power and thrust coefficients signals. The peaks at multiples frequencies correspond to the multiples of $3\,P_r$, highlighted by vertical dashed lines, given the periodicity of the signal and of the passage of the blades. The vertical blue line indicates the first torsional natural frequency of the blade $f = 5.58\,\mathrm{Hz}$ and underlines the peak of the PSD in the ALM/IVT case, especially for the thrust coefficient. ALM —, ALM/IV —, ALM/IVT —.

The time-averaged power and thrust coefficient obtained with rigid ALM and ALM/IV are almost identical (Table 3 and horizontal lines in Figure 5), despite the differences observed before in the instantaneous value of the forces. However, when we also consider the torsion of the airfoil section, the power is significantly reduced, by approximately 5 % with respect to the other two cases. Similarly, the thrust is about 10 % smaller, which could also affect a possible *a posteriori* estimation of the tower deflection [65]. In general, this seems to imply that simulations perfomed considering the blades as infinitely rigid overestimate the power coefficient and also the momentum deficit behind the turbine.

Figure 6 presents the PSD obtained from the time signals of the coefficients, to assess if the coupling procedure affects the frequency content of the power and

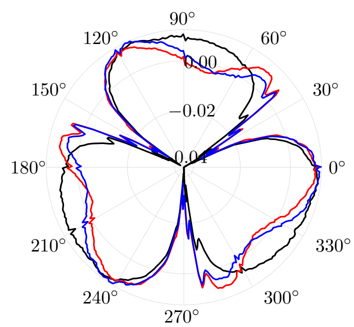

(a) ΔC_P

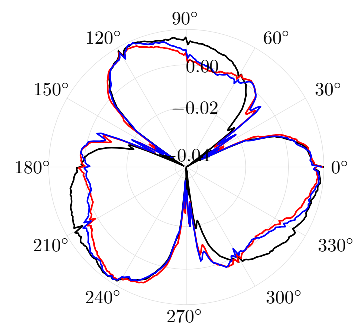

(b) ΔC_T

Figure 7: Polar plots of the phase-averaged power and thrust coefficients fluctuations. ALM —, ALM/IV —, ALM/IVT —

thrust signals. The periodic passage of the three blades and the tower shadow effect induces distinct peaks observable at the frequencies multiple of $3\,P_r$, with P_r being the rotational frequency. The spectral content of the ALM/IV case is almost the same as the one of the ALM case, whereas in the ALM/IVT case, the direct influence of the torsional deformation on the aerodynamic forces adds a small, but distinct, contribution of the first torsional natural frequency of the blades $f = 5.58\,\mathrm{Hz}$ (see Table 1), typical of the torsional vibration, especially to the thrust coefficient.

To investigate the specific effect of the torsional dynamics in addition to the mean value reduction, Figure 7 compares the coefficients fluctuations for the three cases in a polar plot. The plots show that the torsional dynamics, and in particular the oscillation of the torsional angle caused by the tower, produces also a modification in the region between the two following minima of the coefficients compared to the ALM/IV case.

In Figure 8, we also report the Probability Density Function (pdf) of the two coefficients, showing how the coupling procedures redistribute in different ways the torque and the thrust. Obviously, all the results show the presence of an asymmetrical negatively skewed distribution with a peak close to the time-averaged values of the coefficients, related to the undisturbed aerodynamic forces, and a longer tail below the main peak, related to the drops in the coefficients caused

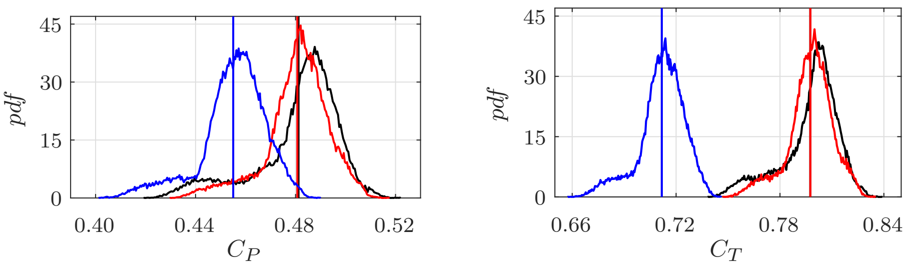

(a) C_P (b) C_T

Figure 8: Probability density function of the power and thrust coefficients. Vertical lines indicate the respective time-averaged values. ALM —, ALM/IV —, ALM/IVT —.

by the tower shadow effect. Except for the different averages, Figure 8 shows that the two-way coupled cases have a mean closer to the mode, *i.e.* the value that appears most often in a set of data values, and a more compact tail below the mean. The absence of the fluctuations in the coefficients that are caused by the aeroelastic coupling makes the tower shadow effect sharper for the ALM case. In fact, the pdf of the one-way coupled case can be considered in the limit as a sort of bimodal distribution with one major peak, related to the condition with no blades in front of the tower, and an other minor peak, related to the condition with one blade in front of it.

4.2. Displacement and deformation velocity

In this section, the structural dynamics of the blades is analysed. Figure 9 and Figure 10 report the phase-averaged displacements and deformation velocities of the six DFs in correspondence of the free edge of the blades. The figures show that the axial (Fig. 9a) and edgewise (Fig. 9c and Fig. 9e) structural dynamics are mainly dominated by gravity, as also reported in other works [29], and thus that they are only slightly affected by the aeroelastic coupling procedure. On the other hand, the flapwise (Fig.9b and Fig.9f) and the torsional (Fig.9d) dynamics are influenced considerably by the aerodynamic forces, and especially by the presence of the tower, which represents the main source of unsteadiness for the structural response of these two DFs. The local reduction in the aerodynamic loading, which produces also the observed drops in the power

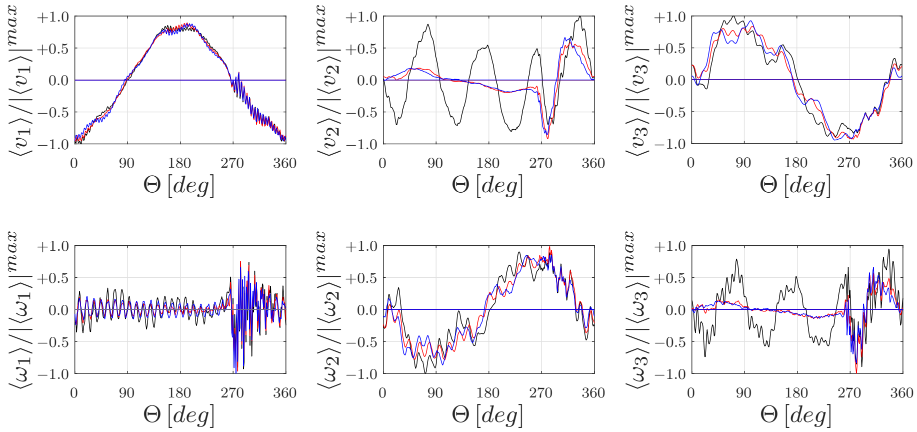

Figure 9: Phase-averaged tip deformation velocity. The curves represent the averages on the three blades. ALM —, ALM/IV —, ALM/IVT —.
The maximum absolute values of the phase-averaged fluctuations used for the normalisations are: $|\langle v_1\rangle|^{max} = 0.0031\, m/s$, $|\langle v_2\rangle|^{max} = 2.42\, m/s$, $|\langle v_3\rangle|^{max} = 0.71\, m/s$, $|\langle \omega_1\rangle|^{max} = 5.29\, deg/s$, $|\langle \omega_2\rangle|^{max} = 1.22\, deg/s$, $|\langle \omega_3\rangle|^{max} = 7.72\, deg/s$

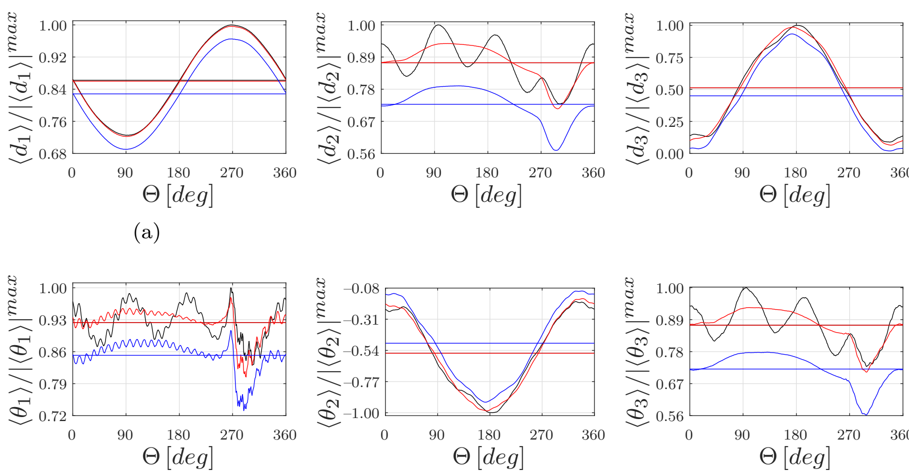

(a)

Figure 10: Phase-averaged tip displacement. The curves represent the averages on the three blades. ALM —, ALM/IV —, ALM/IVT —. The maximum absolute values of the phase-averaged fluctuations used for the normalisations are: $|\langle d_1\rangle|^{max} = 0.015\, m$, $|\langle d_2\rangle|^{max} = 5.45\, m$, $|\langle d_3\rangle|^{max} = 1.06\, m$, $|\langle \theta_1\rangle|^{max} = 2.55\, deg$, $|\langle \theta_2\rangle|^{max} = 1.75\, deg$, $|\langle \theta_3\rangle|^{max} = 12.00\, deg$

and the thrust coefficients, breaks the low-frequency structural vibrations just after the position of the tower at $\Theta = 270°$, given the fact that the structure does not react instantaneously to the sudden change in the forcing, and that

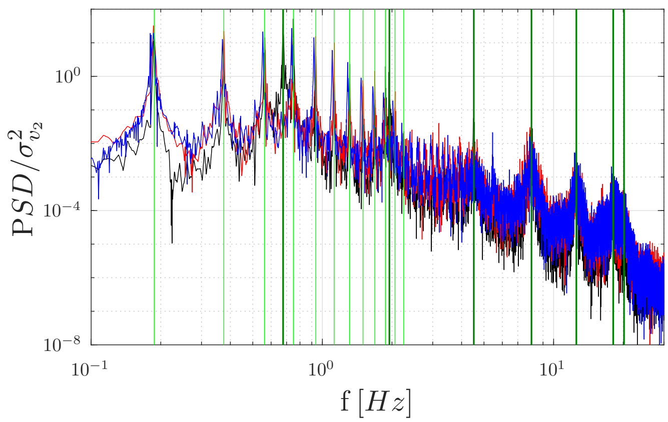

Figure 11: Normalised PSD of the flapwise deformation velocity component v_2 in logarithmic scale. Light green vertical lines denote the first twelve multiples of the mean rotor angular frequency, and indicate the influence of the periodic motion of the rotor. Dark green vertical lines denote the first seven natural frequencies of the modes with dominant flapwise bending features. ALM —, ALM/IV —, ALM/IVT —.

the tower has a certain width.

As a consequence of the larger influence of the aerodynamic forces on the flapwise and torsional structural dynamics, it is evident that these DFs are considerably influenced both in the unsteady and the mean distributions by the instantaneous aeroelastic interaction.

The contribution of the deformation velocity in the definition of the angle of attack dampens the structural response ascribable to the first structural mode, which is essentially a flapwise bending mode with a mild influence on torsion, as also shown in the spectrum of the flapwise deformation velocity v_2 in Figure 11. As a matter of fact, it is known in literature [2] that the aerodynamic damping in flapwise direction is relatively high when the flow is attached, in contrast to the small aerodynamic damping that characterises the edgewise motion. As shown in Figure 12, a positive flapwise deformation velocity induces a negative variation of the angle of attack and of the relative velocity magnitude that finally reduces the aerodynamic forces, and vice versa. Moreover, as shown in Figure 9b, peaks of $\langle v_2 \rangle$ reach relevant values, approximately 20 % of the mean hub velocity, exactly in the region where the presence of the tower and also the sheared mean velocity profile reduce the local absolute velocity in

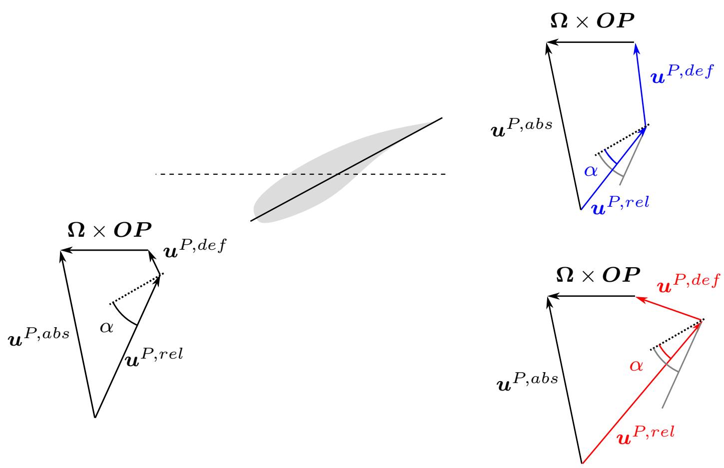

Figure 12: Sketch to highlight the different aerodynamic damping mechanisms for flapwise and edgewise motion. On the left, a generic initial condition with positive deformation velocity components is reported. On the right, we increase the flapwise (top) and edgewise (bottom) deformation velocity components, and we indicate in blue and red respectively the new kinematics. While in the first case both incidence and relative velocity magnitude decrease, in the second case only incidence decreases whereas the relative velocity magnitude increases. Moreover, especially towards the tip of the blade, the rotational velocity dominates the edgewise motion, while the flapwise deformation velocity remains comparable to the streamwise flow velocity throughout blade revolution.

correspondence of the airfoils. As a result, it is clear that the flapwise motion plays a key role in the definition of the local aerodynamic forces and that the one-way coupling approach is unable to describe the resulting flapwise aerodynamic damping.

Conversely, a positive edgewise motion would reduce the angle of attack, but would increase the relative velocity magnitude (Figure 12). However, given the large values of the rotational tangential velocity compared to the small edgewise velocities provided by the structural dynamics, the damping effect of the edgewise motion is much smaller than the flapwise one.

Finally, the blades show a nose-down torsion (Fig.10d) mainly affected by the tower unsteadiness and by the first torsional mode, observable in the high frequency vibrations. The introduction of the torsional deformation in the angle of attack thus reduces in general the aerodynamic forces and, as a consequence, the mean deformations (Figure 10). However, except for the mean value of the deformations, the torsional dynamics of the ALM/IV and ALM/IVT cases

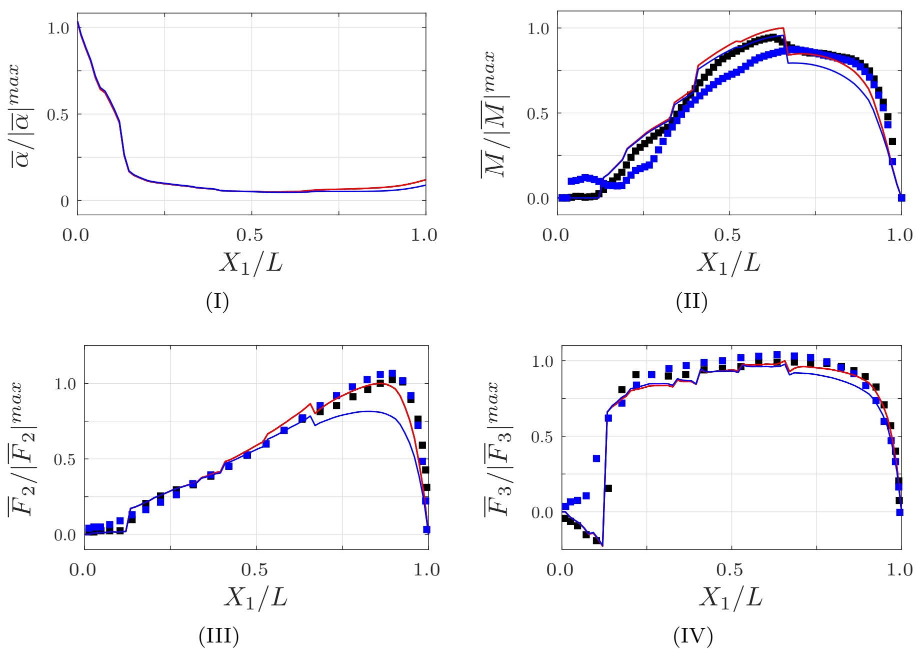

Figure 13: Time-averaged aerodynamic quantities along the blades: I) local incidence; II) aerodynamic moment; III) flapwise aerodynamic force; IV) edgewise aerodynamic force. ALM —, ALM/IV —, ALM/IVT —, ■ HAWC2, ■ Heinz [26]. The ALM curves are not visible because they are exactly behind the ALM/IV curves.
The maximum absolute values of the time-averaged quantities used for the normalisations are: $|\overline{\alpha}|^{max} = 60\, deg$, $|\overline{M}|^{max} = 2550\, N$, $|\overline{F}_2|^{max} = 6090\, N/m$, $|\overline{F}_3|^{max} = 622\, N/m$.

exhibits only minor differences in the first and last quarters of rotation, when the blades rise after having passed in front of the tower.

4.3. Aerodynamic forces

Figure 13 displays the time-averaged aerodynamic quantities along the span of the blades: the local incidence in Figure 13-I, the aerodynamic pitching moment in Figure 13-II, the flapwise aerodynamic force component in Figure 13-III, and the edgewise aerodynamic force component in Figure 13-IV. The results obtained without torsion agree well with the analogous quantities reported in Heinz [26] for the same mean hub velocity. We point out that, compared to this reference, radial discontinuities are present in our case in correspondence of the spanwise transition from one type of airfoil to another. In fact, Heinz [26] adopted a

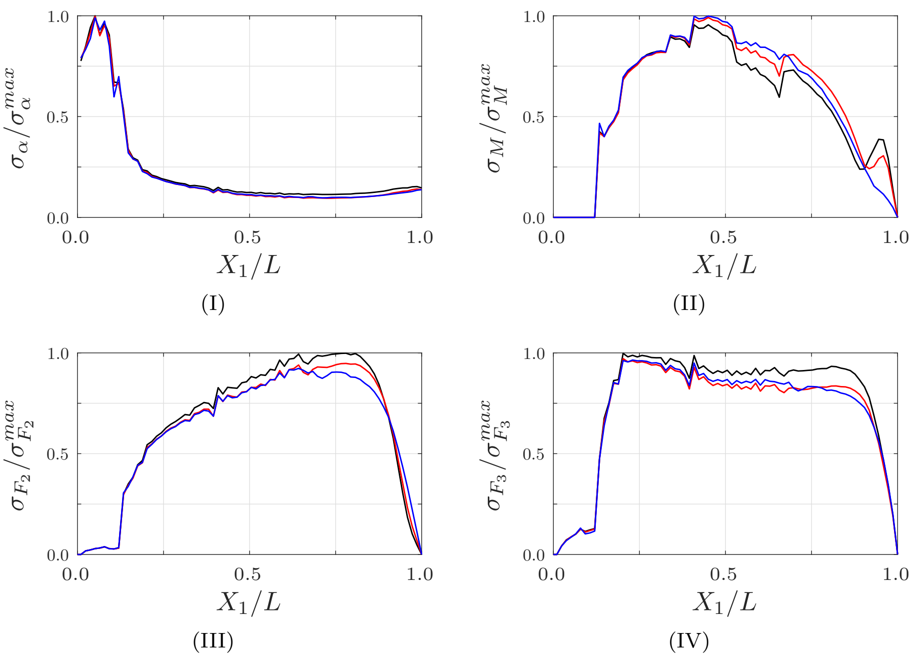

Figure 14: Normalised standard deviation of the aerodynamic quantities along the blades: I) local incidence; II) aerodynamic moment; III) flapwise aerodynamic force; IV) edgewise aerodynamic force. ALM —, ALM/IV —, ALM/IVT —.
The maximum values of the standard deviations used for the normalisations are: $\sigma_\alpha^{max} = 4.70\,deg$, $\sigma_M^{max} = 102\,N$, $\sigma_{F_2}^{max} = 435\,N/m$, $\sigma_{F_3}^{max} = 104\,N/m$.

CFD-CSD approach with body-conformal meshes fitting the blades' geometry. As a result, the smooth 3D surface used by their RANS solver produced smooth distributions of the airloads. On the other hand, the Actuator Line Model uses two-dimensional airfoil data that are not always continuous along the span, and that thus can produce different aerodynamic coefficients even for approximately the same incidence (see Figure 13-I). In fact, the ALM and ALM/IV curves show that the coupling by means of the deformation velocity reduces only slightly the mean incidence, and thus that the induced vibrations of this case have almost a net zero effect for what concerns the aerodynamic forces. On the other hand, the torsional deformation in ALM/IVT, mainly ascribable to the first torsional mode, imposes a monotonically increasing nose-down torsion, which significantly reduces the aerodynamic forces towards the tip of the blade.

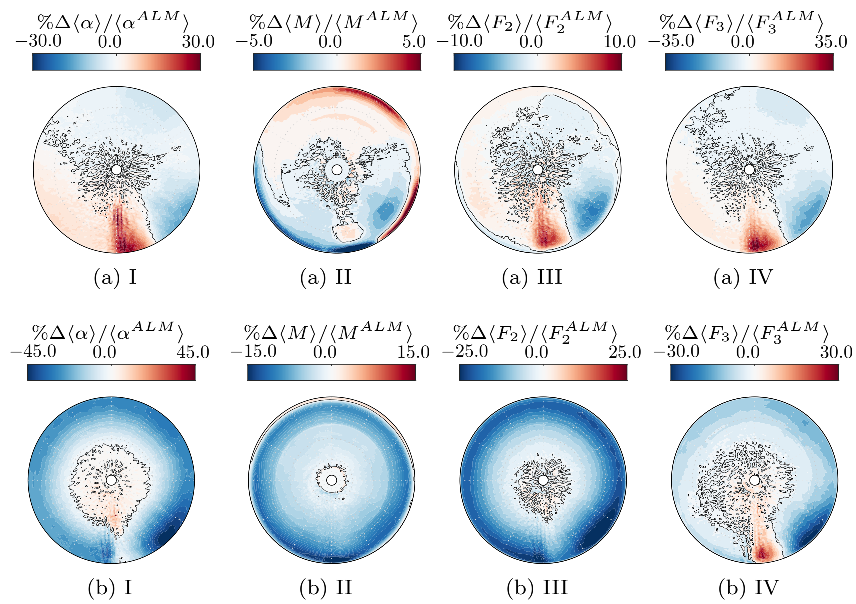

Figure 15: Phase-averaged contours of the percentage differences of the aerodynamic quantities between: a) ALM/IV and ALM case; b) ALM/IVT and ALM case. Differences are normalised with respect to the local values of the ALM case. Iso-lines for null differences are indicated in black. I) Local incidence; II) aerodynamic moment; III) flapwise aerodynamic force; IV) edgewise aerodynamic force.

Despite the mild influence of the two-way coupling procedures on the time averages, the standard deviation of the aerodynamic quantities along the blades in Figure 14 suggests that the FSI modifies the local statistics of the aerodynamic forces, and that the structural motion reduces the dispersive effect of the turbulent fluctuations, especially in the outward region of the blades where the structural vibrations are more important.

To better understand the local behaviour of the aerodynamic loading, we evaluated phase-averaged quantities, better suited than time-averaged ones for describing the effect of the aeroelasticity. Figures 15a report the percentage difference of the phase-averaged aerodynamic quantities of the ALM/IV case with respect to the ones of the ALM case, normalised by the local values of the ALM case itself. The contours show that, while the net effect of the fluctuations is null, a relevant variation takes place in the fourth and last quadrant of revolution. The sudden and abrupt fluctuation of the flapwise deformation velocity, induced by the presence of the tower, causes a relevant change in the local angle of attack, which affects the aerodynamic forces and moment in turn. In fact, by looking at the sign of the flapwise deformation velocity at the tip in Figure 9b and at the sign of the relative difference of the incidence in Figure 15a-I, it can be seen that the azimuthal regions in which the difference is positive correspond to the regions with negative flapwise deformation velocity, which is in accordance with the physical explanation reported in Figure 12.

The distribution of the pitching moment (Figure 15a-II) follows the behaviour imposed by the angle of attack, especially in the bottom part. However, some differences are present. First of all, radial discontinuities reflect the transition from one type of airfoil to the other along the span, given the discontinuous features in terms of pitching moment of the different airfoils, as shown also in Heinz [26]. Second of all, an opposite behaviour is shown in the top part. For the two-way coupled cases in this region, lower aerodynamic forces opposing the fluid allow slightly larger velocities. Provided that the variation of incidence in that region is limited and that the corresponding variation of the pitching moment coefficient is small, the effect of the local increase in the velocity prevails according to Eq. 7 and produces a slight increase in $\langle M \rangle$ in the end.

Figures 15b report the analogous percentage differences for the ALM/IVT case with respect to the ALM case. In general, the behaviour is similar to the one reported in Figures 15a, and the most significant variations are in correspondence of the passage of the blades in front of the tower and in the following quadrant, although the nose-down torsion causes a general reduction of all the aerodynamic quantities. Moreover, the reduced angular velocity of the ALM/IVT case, caused by the smaller loading of the blades, increases slightly the local angle of attack (Fig.15b-I). This is particularly evident in the root region, where the nose-down torsion is still small and thus there is a net increase in the local incidence compared to the ALM case. However, proceeding towards the tip, the torsional deformation becomes more important and affects relevantly the distribution of the angle of attack. This causes a significant de-

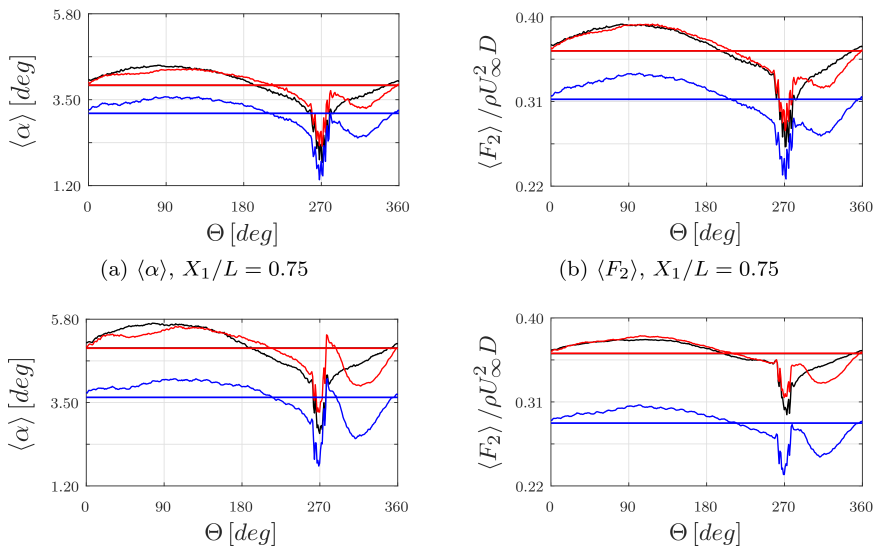

(a) $\langle \alpha \rangle$, $X_1/L = 0.75$

(b) $\langle F_2 \rangle$, $X_1/L = 0.75$

(c) $\langle \alpha \rangle$, $X_1/L = 0.9$

(d) $\langle F_2 \rangle$, $X_1/L = 0.9$

Figure 16: Phase-averaged incidence and flapwise aerodynamic force at radial positions from the hub $X_1/L = 0.75$ and $X_1/L = 0.91$. ALM —, ALM/IV —, ALM/IVT —

crease in the aerodynamic forces in the outer part of the blades, which are the parts contributing the most to the the aerodynamic torque and thrust.

Finally, Figure 16 reports the phase-averaged angle of attack and aerodynamic flapwise force for some radial sections. Apart from the mean value, the figure reveals also that the more complete structural state of the ALM/IVT case introduces another small contribution to the general dynamics of the problem, as shown by the different recovery of the curves from the minimum in correspondence of the tower.

4.4. Reactions

To complete the structural analysis of the results, we analyse the behaviour of the root reactions. In particular, we name R_i the reaction force along the i-th axis of the structural FOR $\mathcal{R}_E$, and M_i^R the reaction moment around the same axis, with sign defined in accordance with the right-hand rule (see Figure 1). Figure 17 reports the phase-averaged reactions and their correspondent time averages for all the 6 DFs in correspondence of the root. The curves confirm

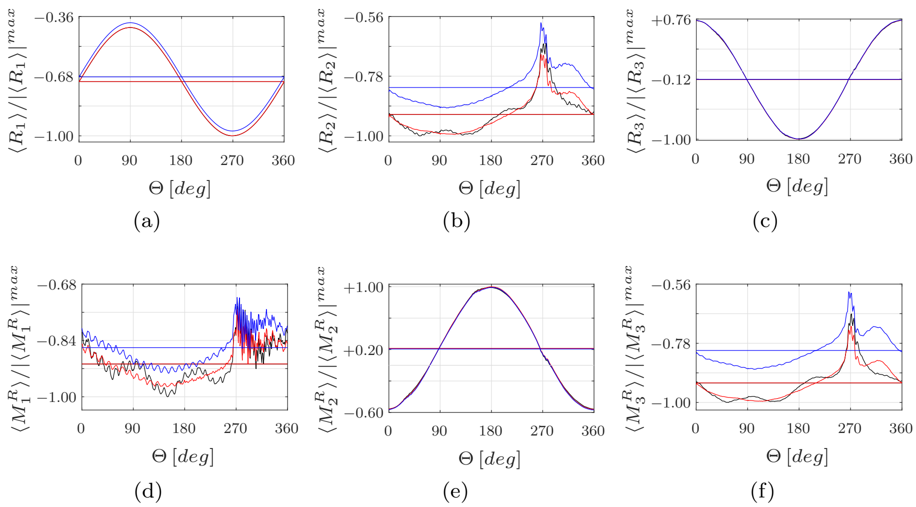

Figure 17: Phase-averaged root reaction components. Horizontal lines indicate the corresponding time-averaged values. ALM —, ALM/IV —, ALM/IVT —.
The maximum absolute values of the phase-averaged quantities used for the normalisations are: $|\langle R_1\rangle|^{max} = 5.95 \cdot 10^5\, N$, $|\langle R_2\rangle|^{max} = 2.18 \cdot 10^5\, N$, $|\langle R_3\rangle|^{max} = 2.00 \cdot 10^5\, N$, $|\langle M_1^R\rangle|^{max} = 9.77 \cdot 10^4\, N\, m$, $|\langle M_2^R\rangle|^{max} = 4.58 \cdot 10^6\, N\, m$, $|\langle M_3^R\rangle|^{max} = 8.69 \cdot 10^6\, N\, m$,

the predominance of the gravitational force on the axial and edgewise DFs (Fig.17a, Fig.17c and Fig.17e respectively), in spite of the torsional and flapwise ones (Fig.17d, Fig.17b and Fig.17f respectively) which are more affected by the aerodynamic forces, and thus are more influenced by the FSI coupling. Furthermore, the high mean value of the axial reaction component reveals the almost constant centrifugal force acting radially.
In addition to generally reduced values because of the diminished aerodynamic loads, the ALM/IVT case presents also a small phase shift after the tower azimuthal position, where the torsional dynamics imposes a faster recovery of the aerodynamic loads than in the ALM/IV case (see also Figure 7). Finally, the time-averaged values differ only in the ALM/IVT case, and are in line with other studies with similar flow conditions [44], confirming the general validity of our model.

Given the highly unsteady loads imposed by the fluctuating wind conditions, it is critical to evaluate the fatigue properties of the structure and to assess the

Table 4: Percentage difference of root reaction DELs for the ALM/IV and ALM/IVT cases with respect to the ALM case. The percentage difference for the generic root reaction component R_i is defined as $\Delta R_i\% = 100 \cdot (DEL_{R_i} - DEL_{R_i}^{ALM})/DEL_{R_i}^{ALM}$, where DEL_{R_i} is the Damage Equivalent Load of the two-way coupled case considered, and $DEL_{R_i}^{ALM}$ is that of the one-way coupled case.

DEL	$\Delta R_1\,\%$	$\Delta R_2\,\%$	$\Delta R_3\,\%$	$\Delta M_1^R\,\%$	$\Delta M_2^R\,\%$	$\Delta M_3^R\,\%$
ALM/IV	0.00 %	−14.19 %	+0.31 %	−23.33 %	+0.74 %	−15.57 %
ALM/IVT	−0.17 %	− 8.68 %	+0.03 %	− 7.28 %	+0.41 %	−11.58 %

effect of the aeroelastic coupling procedures on them. Among the different possible characterisations, a widely used measure of the impact of the fatigue loads on the structure is the Damage Equivalent Load (DEL) [66], which represents the amplitude of the single constant-rate alternating load that produces the same total damage of the real load spectrum.

We evaluated the DELs for the reactions of each case by means of the post-processing tool MCrunch [67]. The tool counts the cycles by means of the widely used rainflow counting algorithm [68], adopts the linear Palmgren-Miner rule for damage accumulation [69], and uses standard S-N fitting curves to characterise the material behaviour, for which we chose a constant slope, typical of composite materials, equal to 10.

Table 4 reports the percentage differences of the two-way coupled cases with respect to the one-way coupled case. The results show that, in general, the one-way coupled simulation overestimates the fluctuations of the loads, and that the aerodynamic damping caused by the introduction of the deformation velocity limits the low-frequency fluctuations of the blade loading. Furthermore, the ALM/IVT case shows only a slightly larger DEL than the ALM/IV case, especially in the torsional root reaction component $DEL(M_1^R)$. In fact, the direct influence of the high-frequency/small-amplitude torsional oscillation in the ALM/IVT case induces fluctuations that are slightly more relevant for this component, as shown in Figure 17d. On the other hand, the small amplitude of the torsional angle fluctuations in this case is insufficient to affect the low frequency unsteadiness of the gravity and the aerodynamic loads in edgewise

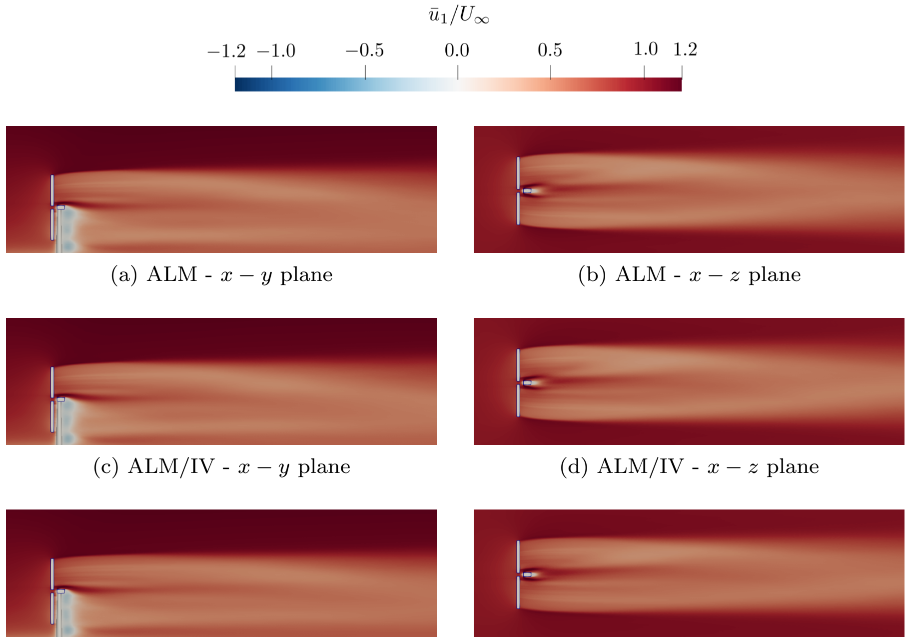

(a) ALM - $x-y$ plane

(b) ALM - $x-z$ plane

(c) ALM/IV - $x-y$ plane

(d) ALM/IV - $x-z$ plane

(e) ALM/IVT - $x-y$ plane

(f) ALM/IVT - $x-z$ plane

Figure 18: Time-averaged streamwise velocity on a vertical slice through the wind turbine centre (left) and on a horizontal slice at hub height (right).

and flapwise directions respectively.

4.5. Fluid flow analysis

As a final step, we analyse the fluid variables. Figure 18 shows the time-averaged streamwise velocity component on a vertical slice through the turbine centre and on a horizontal slice at hub height for the three cases. In the vertical plane, it can be seen that the action of the blades decelerates the flow, while the tower induces a recirculation region behind the turbine, which thus breaks the symmetry of the flow between the bottom and the top part of the rotor. In particular, the region of reversed flow is divided into three parts: a lower part, behind the section of the tower uncovered by the blades, an intermediate part, behind the section of the tower covered by the external half of the rotor, and a higher part, behind the nacelle and the section of the tower covered by the internal half of the rotor. While the bottom part is only affected by the undisturbed flow, the intermediate part is influenced by the presence of the blades, and indeed its longitudinal extent is reduced by the upstream deceleration imposed by the rotor to the fluid. Finally, the higher part has again a larger extent, because of the larger longitudinal size of the nacelle compared to the tower, and because of the higher fluid velocity at hub height and above.

Furthermore, an asymmetric behaviour of the wake is shown also in the horizontal plane. In fact, the tower and the nacelle obstruct the flow and induce a Von Kármán vortex street, which is tilted by the helical motion given by the revolution of the blades, as already shown in Santoni et al. [57].

However, from the comparison of the three cases, no significant difference can be observed, except for some very small quantitative changes in the ALM/IVT case caused by the reduced aerodynamic forces.

Finally, we compare the instantaneous coherent structures of the flow for a generic instant with $\Theta = 90°$, represented by means of the Q-criterion [70] in Figure 19. The root vortices generated close to the hub are promptly disrupted by their interaction with the wake of the nacelle, whereas the tip vortices are dissipated after approximately one diameter from the tower. As expected, the mild wind shear imposed, and thus the different convection velocity of the vortices at different heights, causes only a modest change in slope of the helical structures in the wake that is slightly visible from the lateral views. On the horizontal slice at the tower base instead, it is possible to appreciate the trace of the induced Von Kármán vortex street generated by the tower obstruction. The comparison of the isosurfaces in Figure 19 shows that the three cases under study are essentially similar. However, as we already commented, the reduced forces along the blades in the ALM/IVT case cause thinner and less intense tip vortices. Moreover, the reduced angular velocity increased the pitch of the helical wake structure.

Ultimately, we can conclude that our simulations suggests that from the point of view of the fluid dynamics, the aeroelastic coupling for the reference turbine under study has a small effect, limited to the very near wake only.

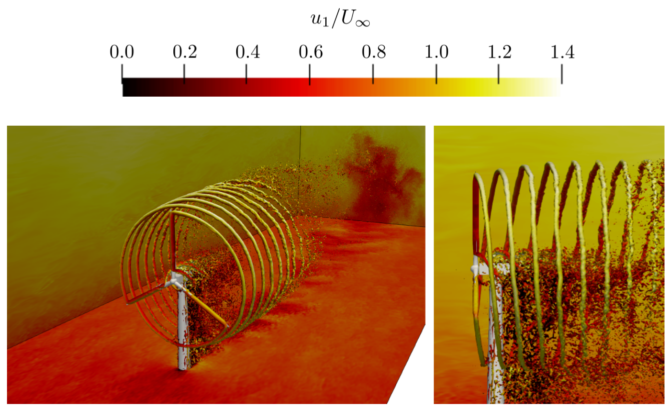

(a) ALM

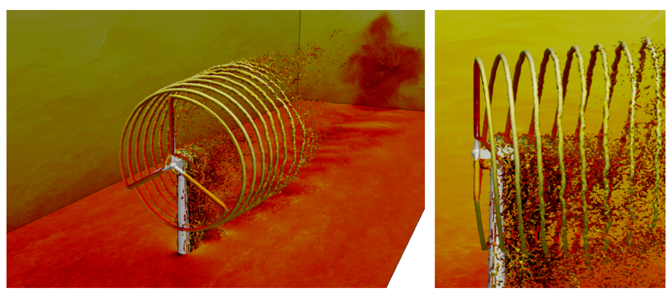

(b) ALM/IV

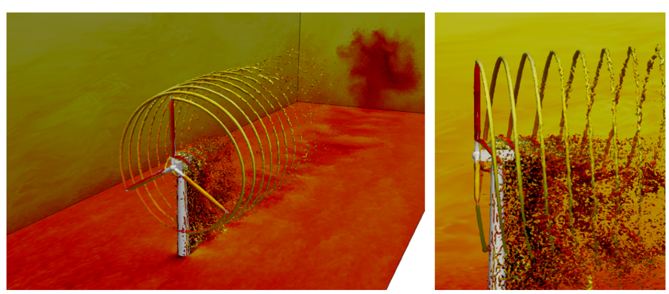

(c) ALM/IVT

Figure 19: Instantaneous isosurface of the Q-criterion variable coloured by the streamwise velocity. Three-point perspective projection of the field on the left, and lateral view on the $x-y$ plane on the right.

5. Conclusions

In this work, we presented a novel high-fidelity CFD-CSD model for the study of the aeroelastic response of wind turbines. The CFD solver adopts an

LES approach modelling the rotor by means of the Actuator Line Model, and the tower and the nacelle by means of an Immersed Boundary Method. On the other hand, the CSD solver adopts a modal approach modelling the blades only as rotating cantilever beams, and includes the inertial effects in modal basis by means of the method followed by Saltari et al [61]. The coupling adopted is loose and staggered, to avoid undermining the computational efficiency of the complete coupled scheme, and takes advantage of the sectional evaluation of the aerodynamic forces of ALM, which thus provides a natural and efficient interface between the two physical subproblems.

Hence, for the NREL 5 MW wind turbine under turbulent sheared conditions, we compared the results of three sets of simulations that we named ALM, ALM/IV, and ALM/IVT. In the first case, we considered only a one-way coupling approach in which the LES solver provided the aerodynamic loading to the structural solver running in parallel; in the second case, we introduced in the definition of the local angle of attack a first structural feedback, made of the instantaneous bending deformation velocity in and out of the plane; in the third case, we added also the instantaneous torsional deformation caused by the unsteady loads to the structural feedback.

The results show that:

- The dynamics of the deformation velocity introduces an important variation in terms of power production, loads distribution, structural dynamics and fatigue properties. In particular, the dynamics of the flapwise deformation velocity introduces a relevant aeroelastic damping that the one-way coupled simulations are not able to capture. The effect of the edgewise deformation velocity, instead, besides being ambiguous, is overshadowed by the larger rotational velocity.

- The effect of the torsional dynamics in the ALM/IVT case, often neglected in the literature, impacts significantly the estimated performances. In particular, the mean nose-down deformation of the blades reduces the aerodynamic loads, which thus suggests an overestimation of the generated power when adopting one-way coupled simulations. The dynamic effect of the torsional fluctuations instead is in general modest and, although some small effects on the other DFs and on the root reactions start to be visible, the amplitude of the vibrations is still not sufficient to cause substantial differences for the turbine considered. However, different studies [34] have shown that the NREL 5 MW wind turbine has rather stiff blades. Thus, for longer and more flexible blades, it is not excluded that torsional dynamics could play a more influential role in FSI.

- The presence of the tower is key to predicting correctly the fluid and structural dynamics. On the one hand, it breaks the symmetry of the fluid field and the coherence of the wake structures; on the other hand, it is the main source of unsteadiness in the structural dynamics. Moreover, the reduced aerodynamic loads caused by the tower draw attention to the the effect of the aeroelastic coupling, which is amplified by the large vibrations of the structure in the quarter of revolution following the tower itself. However, given the strong influence of the various features of the atmospheric flow on the turbine performance [71, 72], further in-depth analysis must be carried out to better characterise the turbine aeroelastic response for different and more realistic turbulent inflows. Indeed, turbulence intensity in our cases was rather low, and more intense turbulent structures could affect significantly the coupled dynamics and even dominate the tower-induced unsteadiness.

- The flapwise and the torsional vibrations are those more affected by the aerodynamic loads and thus by the FSI coupling mechanisms under study. On the contrary, the axial and edgewise DFs are mainly affected by the gravitational force, given the large mass of each blade, as shown also in other works [28].

- While the structural dynamics, the aerodynamic loads, and the wind turbine coefficients show the effects of the different coupling procedures, the fluid field quantities are less or in no way sensitive to them.

The time-averaged results were in general in good agreement with similar studies with different techniques, but the inherent features of our high-fidelity CFD-CSD approach accurately provided additional information also on the unsteady and distinct effects of the coupling procedures. The present work thus explicitly assessed the unsteady impact of the aeroelastic mechanisms on a utility-scale wind turbine under turbulent operative conditions, simulated by means of a simplified but accurate numerical rotor modelling.

Moreover, several studies [73, 74] have demonstrated the capability of LES solvers to simulate numerically the effects of the fluid interaction between turbines in realistic layouts of wind farms, but under the assumption of rigid structures. The presented method will allow us in future works to assess also the aeroelastic effects on the loading of the turbines in similar waked operational regimes. Finally, experimental measurements [75] have shown the effects, also for wind turbine blades, of the complex and 3D unsteady aerodynamics. Under highly variable operational conditions and turbulent inflows, it is thus reasonable to think that our future implementation of a dynamic stall model could potentially affect also the aeroelastic interaction.

Acknowledgments

We acknowledge the Texas Advanced Computing Center (TACC) for having provided us with the computational resources required by this work.
We kindly thank F. Saltari for the helpful discussion on the structural solver and the structural analysis, and U. Ciri for the help with the fluid solver and for his precious know-how in wind energy.

Appendix A. Derivation of the fully-coupled equations of motion for a moving flexible blade

The general fully-coupled equations of motion for a rotating flexible blade are here obtained from a weak formulation of the Cauchy's equation, also known as virtual work principle, that includes the rigid-body and the linear elastic dynamics. By multiplying the Cauchy equations by a generic virtual displacement $\delta\boldsymbol{x}$ for a flexible continuous structure, and by integrating on the volume $\mathcal{V}$ occupied by the structure, we obtain

$$\iiint_{\mathcal{V}} \rho_s \boldsymbol{a}_s \cdot \delta\boldsymbol{x}\, \mathrm{d}\mathcal{V} = \iiint_{\mathcal{V}} \rho_s \boldsymbol{f}_s \cdot \delta\boldsymbol{x}\, \mathrm{d}\mathcal{V} + \iint_{\mathcal{S}} \boldsymbol{t}_s \cdot \delta\boldsymbol{x}\, \mathrm{d}\mathcal{S} - \iiint_{\mathcal{V}} \boldsymbol{T}_s : \delta\boldsymbol{E}\, \mathrm{d}\mathcal{V}, \tag{A.1}$$

where $\boldsymbol{a}_s = \mathrm{D}\boldsymbol{v}/\mathrm{D}t$ is the body acceleration, $\boldsymbol{f}_s$ and $\boldsymbol{t}_s$ are the external forces per unit volume and surface, $\boldsymbol{T}_s$ is the stress tensor in the body, $\delta\boldsymbol{E}$ is the virtual strain increment tensor, and $\mathcal{S}$ is the exterior surface of the structural volume $\mathcal{V}$.

The virtual displacement $\delta\boldsymbol{x}$ is expressed as a combination of the elastic motion and the rigid-body motion of the generic point at distance $\boldsymbol{r}$ from the centre O' of the relative FOR, which moves with angular speed $\boldsymbol{\Omega}$ and $\dot{\boldsymbol{\Omega}}$ with respect to the fixed FOR fixed in O. In our case, for example, O' corresponds to the root of the blade, and O corresponds to the centre of the hub. Thus, we have that

$$\delta\boldsymbol{x} = \delta\boldsymbol{x}_{O'} + \delta\boldsymbol{\Theta} \times \boldsymbol{r} + \sum_{n=1}^{\infty} \delta q_n \boldsymbol{\psi}^n, \tag{A.2}$$

where $\delta\boldsymbol{x}_{O'} + \delta\boldsymbol{\Theta} \times \boldsymbol{r}$ is the virtual rigid-body motion contribution, made up of a translational part and a (rigid) rotational part, whereas the last contribution is the virtual elastic deformation $\delta\boldsymbol{d}$, described in terms of shape functions $\boldsymbol{\psi}^n(\boldsymbol{x})$.

Hence, the first term on the left-hand side can be expressed as

$$\delta\boldsymbol{x}_{O'} \cdot \iiint_{\mathcal{V}} \rho_s \boldsymbol{a} \mathrm{d}\mathcal{V} + \delta\boldsymbol{\Theta} \cdot \iiint_{\mathcal{V}} \rho_s \boldsymbol{r} \times \boldsymbol{a} \mathrm{d}\mathcal{V} + \sum_{n=1}^{\infty} \delta q_n \iiint_{\mathcal{V}} \rho_s \boldsymbol{a} \cdot \boldsymbol{\psi}^n \mathrm{d}\mathcal{V}, \tag{A.3}$$

and then the three integrals in the above formula can be recast as follows:

- according to the Reynolds transport theorem, the first integral becomes

$$\iiint_{\mathcal{V}} \rho_s \frac{\mathrm{D}\boldsymbol{v}}{\mathrm{D}t} \mathrm{d}\mathcal{V} = \frac{\mathrm{d}}{\mathrm{d}t} \iiint_{\mathcal{V}} \rho_s \boldsymbol{v} \mathrm{d}\mathcal{V} = m_t \frac{\mathrm{d}\boldsymbol{v}_G}{\mathrm{d}t} \tag{A.4}$$

  where m_t is the total mass of the body and $\boldsymbol{v}_G$ is the absolute velocity of the centre of mass.

- By defining the relative velocity with respect to the centre of mass $\boldsymbol{v}' = \boldsymbol{v} - \boldsymbol{v}_G$, and the position of the centre of mass of the structure in the relative FOR $\boldsymbol{r_{O'G}}$, such that $\boldsymbol{r} = \boldsymbol{r_{O'G}} + \boldsymbol{r_g}$, the second integral becomes

$$
\begin{aligned}
&\iiint_{\mathcal{V}} \rho_s \boldsymbol{r} \times \frac{\mathrm{D}\boldsymbol{v}}{\mathrm{D}t} \mathrm{d}\mathcal{V} = \\
&\quad = \iiint_{\mathcal{V}} \rho_s \boldsymbol{r_{O'G}} \times \frac{\mathrm{D}\boldsymbol{v}}{\mathrm{D}t} \mathrm{d}\mathcal{V} + \iiint_{\mathcal{V}} \rho_s \boldsymbol{r_g} \times \frac{\mathrm{D}\boldsymbol{v}}{\mathrm{D}t} \mathrm{d}\mathcal{V} = \\
&\quad = \iiint_{\mathcal{V}} \rho_s \boldsymbol{r_{O'G}} \times \frac{\mathrm{D}\boldsymbol{v}}{\mathrm{D}t} \mathrm{d}\mathcal{V} + \iiint_{\mathcal{V}} \rho_s \boldsymbol{r_g} \times \frac{\mathrm{D}\boldsymbol{v}'}{\mathrm{D}t} \mathrm{d}\mathcal{V} = \\
&\quad = \boldsymbol{r_{O'G}} \times \iiint_{\mathcal{V}} \rho_s \frac{\mathrm{D}\boldsymbol{v}}{\mathrm{D}t} \mathrm{d}\mathcal{V} + \iiint_{\mathcal{V}} \rho_s \frac{\mathrm{D}}{\mathrm{D}t} \left(\boldsymbol{r_g} \times \boldsymbol{v}'\right) \mathrm{d}\mathcal{V} = \\
&\quad = m_t \, \boldsymbol{r_{O'G}} \times \frac{\mathrm{d}\boldsymbol{v_G}}{\mathrm{d}t} + \frac{\mathrm{d}\boldsymbol{h}_G}{\mathrm{d}t}
\end{aligned}
\tag{A.5}
$$

where $\boldsymbol{h}_G$ is the angular momentum of the structure with respect to the centre of mass.

- In the last integral, we can express the absolute acceleration $\boldsymbol{a}$ in terms of its components when described in the moving FOR:

$$
\boldsymbol{a} = \underbrace{\boldsymbol{a_{rel}}}_{\text{Relative acc.}} + \underbrace{\boldsymbol{a_{O'}}}_{\text{O' acc.}} + \underbrace{\boldsymbol{\Omega} \times (\boldsymbol{\Omega} \times \boldsymbol{r_{rel}})}_{\text{Centrifugal acc.}} + \underbrace{\dot{\boldsymbol{\Omega}} \times \boldsymbol{r_{rel}}}_{\text{Euler acc.}} + \underbrace{2\boldsymbol{\Omega} \times \boldsymbol{v_{rel}}}_{\text{Coriolis acc.}}, \tag{A.6}
$$

where $\boldsymbol{r_{rel}}$, $\boldsymbol{v_{rel}}$ and $\boldsymbol{a_{rel}}$ are respectively the position, the velocity and the acceleration of a generic point in the relative FOR, $\boldsymbol{a_{O'}}$ is the acceleration of the origin O' with respect to the origin of the fixed FOR O, $\boldsymbol{\Omega} \times (\boldsymbol{\Omega} \times \boldsymbol{r_{rel}})$ is the centrifugal acceleration, $\frac{\mathrm{d}\boldsymbol{\Omega}}{\mathrm{d}t} \times \boldsymbol{r_{rel}}$ is the Euler acceleration, and $2\boldsymbol{\Omega} \times \boldsymbol{v_{rel}}$ is the Coriolis acceleration.
By assuming undeformable tower and nacelle, the moving origin acceleration is determined only by the angular speed and acceleration, and its undeformed position $\boldsymbol{R_{O'}}$:

$$
\boldsymbol{a_{O'}} = \frac{\mathrm{d}\boldsymbol{R_{O'}}}{\mathrm{d}t} = \dot{\boldsymbol{\Omega}} \times \boldsymbol{R_{O'}} + \boldsymbol{\Omega} \times (\boldsymbol{\Omega} \times \boldsymbol{R_{O'}}) \,. \tag{A.7}
$$

Given the distributive property of the vector product over addition, we can group these two terms in the Euler and centrifugal acceleration terms respectively, where we use $\boldsymbol{r} = \boldsymbol{R_{O'}} + \boldsymbol{R_{O'P}} + \boldsymbol{d} = \boldsymbol{R_{OP}} + \boldsymbol{d}$. Moreover, we have that $\boldsymbol{v_{rel}} = \dot{\boldsymbol{d}}$, and $\boldsymbol{a_{rel}} = \ddot{\boldsymbol{d}}$.

Thus, by leveraging the vector triple product formula, the n-th term from the centrifugal term gives:

$$\begin{aligned}
&\iiint_{\mathcal{V}} \rho_s \boldsymbol{\Omega} \times (\boldsymbol{\Omega} \times \boldsymbol{r}) \cdot \boldsymbol{\psi}^n \mathrm{d}\mathcal{V} = \\
&\qquad = -\boldsymbol{\Omega} \cdot \mathrm{sym} \left\{ \iiint_{\mathcal{V}} \rho_s \left[(\boldsymbol{R}_{OP} \cdot \boldsymbol{\psi}^n)\, \mathbf{I} - \boldsymbol{R}_{OP} \otimes \boldsymbol{\psi}^n \right] \mathrm{dV} \right\} \boldsymbol{\Omega} + \\
&\qquad - \sum_{m=1}^{\infty} \boldsymbol{\Omega} \cdot \mathrm{sym} \left\{ \iiint_{\mathcal{V}} \rho_s \left[(\boldsymbol{\psi}^m \cdot \boldsymbol{\psi}^n)\, \mathbf{I} - \boldsymbol{\psi}^m \otimes \boldsymbol{\psi}^n \right] \mathrm{dV} \right\} \boldsymbol{\Omega}\, q_m = \\
&\qquad = -e_n^c + \sum_{m=1}^{\infty} K_{nm}^c q_m \, ,
\end{aligned} \tag{A.8}$$

by leveraging the scalar triple product, the n-th term from the Euler term gives:

$$\begin{aligned}
&\iiint_{\mathcal{V}} \rho_s \left(\dot{\boldsymbol{\Omega}} \times \boldsymbol{r} \right) \cdot \boldsymbol{\psi}^n \mathrm{d}\mathcal{V} = \\
&\qquad = \dot{\boldsymbol{\Omega}} \cdot \iiint_{\mathcal{V}} \rho_s \left(\boldsymbol{R_{OP}} \times \boldsymbol{\psi}^n \right) \mathrm{d}\mathcal{V} + \\
&\qquad + \sum_{m=1}^{\infty} \dot{\boldsymbol{\Omega}} \cdot \iiint_{\mathcal{V}} \rho_s \left(\boldsymbol{\psi}^m \times \boldsymbol{\psi}^n \right) \mathrm{dV}\, q_m = \\
&\qquad = -e_n^{Eu} + \sum_{m=1}^{\infty} K_{nm}^{Eu} q_m \, ,
\end{aligned} \tag{A.9}$$

the n-th term from the Coriolis term gives:

$$\begin{aligned}\iiint_{\mathcal{V}} \rho_s 2\, (\boldsymbol{\Omega} \times \boldsymbol{v_{rel}}) \cdot \boldsymbol{\psi}^n \mathrm{d}\mathcal{V} &= \\ &= \sum_{m=1}^{\infty} 2\, \boldsymbol{\Omega} \cdot \iiint_{\mathcal{V}} \rho_s\, (\boldsymbol{\psi}^m \times \boldsymbol{\psi}^n)\, \mathrm{dV}\, \dot{q}_m = \\ &= \sum_{m=1}^{\infty} D^{Co}_{nm} \dot{q}_m \,,\end{aligned} \tag{A.10}$$

the n-th term from the relative acceleration term gives:

$$\iiint_{\mathcal{V}} \rho_s \boldsymbol{a_{rel}} \cdot \boldsymbol{\psi}^n \,\mathrm{d}\mathcal{V} = \sum_{m=1}^{\infty} M_{nm} \ddot{q}_m \,. \tag{A.11}$$

The projection on the virtual displacement of the first two terms of the right-hand side of Eq. A.1 gives us the action of the external forces:

$$\iiint_{\mathcal{V}} \rho_s \boldsymbol{f}_s \cdot \delta\boldsymbol{x} \,\mathrm{d}\mathcal{V} + \iint_{\mathcal{S}} \boldsymbol{t}_s \cdot \delta\boldsymbol{x} \,\mathrm{d}\mathcal{S} = \boldsymbol{f}_T \cdot \delta\boldsymbol{x}_{O'} + \boldsymbol{m}_{O'} \cdot \delta\boldsymbol{\Theta} + \sum_{n=1} e_n \delta q_n \,. \tag{A.12}$$

where $\boldsymbol{f}_T$ and $\boldsymbol{m}_{O'}$ are the resulting force and moment respectively acting on the structure.

On the other hand, by assuming a linear elastic solid, the last term expresses the structural stiffness contribution to the elastic dynamics

$$\iiint_{\mathcal{V}} \boldsymbol{T}_s : \delta\boldsymbol{E} \,\mathrm{d}\mathcal{V}, = \sum_{n=1}^{\infty} \sum_{m=1}^{\infty} K_{nm} q_m \delta q_n \,. \tag{A.13}$$

Finally, we obtain the following form of Eq. A.1:

$$\begin{aligned}&\left(m_t \frac{\mathrm{d}\boldsymbol{v}_G}{\mathrm{d}t} - \boldsymbol{f}_T\right) \cdot \delta\boldsymbol{x}_{O'} + \left(m_t\, \boldsymbol{r_{O'G}} \times \frac{\mathrm{d}\boldsymbol{v_G}}{\mathrm{d}t} + \frac{\mathrm{d}\boldsymbol{h}_G}{\mathrm{d}t} - \boldsymbol{m}_{O'}\right) \cdot \delta\boldsymbol{\Theta} + \\ &\quad + \sum_{n=1}^{\infty} \delta q_n \left\{ \sum_{m=1}^{\infty} \left[M_{mn} \ddot{q}_m + D^{Co}_{mn} \dot{q}_m + \left(K_{mn} + K^c_{mn} + K^{Eu}_{mn}\right) q_m \right] + \right. \\ &\qquad\qquad\qquad\qquad\qquad\qquad \left. - e_n - e^c_n - e^{Eu}_n \right\}\end{aligned} \tag{A.14}$$

For a general displacement, the fully-coupled equations for a moving flexible body are

$$m_t \frac{\mathrm{d}\boldsymbol{v}_G}{\mathrm{d}t} = \boldsymbol{f}_T \tag{A.15}$$

$$m_t\, \boldsymbol{r_{O'G}} \times \frac{\mathrm{d}\boldsymbol{v_G}}{\mathrm{d}t} + \frac{\mathrm{d}\boldsymbol{h}_G}{\mathrm{d}t} = \boldsymbol{m}_{O'} \quad \Longrightarrow \quad \frac{\mathrm{d}\boldsymbol{h}_G}{\mathrm{d}t} = \boldsymbol{m}_G \tag{A.16}$$

$$\sum_{m=1}^{\infty} \left[M_{nm}\ddot{q}_m + D^{Co}_{nm}\dot{q}_m + \left(K_{nm} + K^c_{nm} + K^{Eu}_{nm}\right) q_m \right] = e_n + e^c_n + e^{Eu}_n \tag{A.17}$$

The above equations fully account for the two-way coupling between the elastic and the rigid-body motion, by means of the inertial coupling terms in the elastic dynamics and by means of the modifications of the inertia caused by the elastic displacement. However, as stated above, we neglect the latter effect, and we consider only the one-way coupling in the elastic dynamics.

The local offset of the centre of mass of each section with respect to the neutral axis is included in the mass matrix by means of the method presented in Reschke [60], which adds diagonal and off-diagonal terms to the lumped mass matrix used in this study.

To represent the inertial coupling terms in Eq. 11, we use a discretisation approach similar to Saltari et al. [61], although in our case the origin is centred at the root of each blade and not in the centre of mass of the structure as in the original reference. The only information required by this method can be obtained from the finite element model of the structure. The main steps of the method are:

1. the integrals in the inertial coupling terms are split up as a sum of integrals on complementary subvolumes $\mathcal{V}_i$ with $i = 1, \dots N$, where N is the number of nodes of the structure. The absolute vector decomposition $\boldsymbol{R}_{OP_i} = \boldsymbol{R}_{g_i} + \boldsymbol{\zeta}$ identifies each generic point in the i-th subvolume, where $\boldsymbol{R}_{g_i}$ is the absolute vector position of the centre of mass of $\mathcal{V}_i$.
2. The following inertia properties of the subvolumes are inferred from the

finite element model:

$$m_i \coloneqq \iiint_{\mathcal{V}_i} \rho_s \, \mathrm{d}\mathcal{V} \,, \tag{A.18}$$

$$\boldsymbol{J}_{g_i} \coloneqq \iiint_{\mathcal{V}_i} \rho_s \, [(\boldsymbol{\zeta} \cdot \boldsymbol{\zeta})\mathbf{I} - \boldsymbol{\zeta} \otimes \boldsymbol{\zeta}] \, \mathrm{d}\mathcal{V} = \iiint_{\mathcal{V}_i} \rho_s (\boldsymbol{\zeta} \cdot \boldsymbol{\zeta})\mathbf{I} \, \mathrm{d}\mathcal{V} + \boldsymbol{J}^{\delta}_{g_i} \tag{A.19}$$

where $\boldsymbol{J}^{\delta}_{g_i}$ is the local inertia tensor $\boldsymbol{J}_{g_i}$ with respect to the local centre of mass minus half of its trace.

3. The local displacement field of the n-th mode shape $\boldsymbol{\psi^n}|_{\boldsymbol{x}}$ is assumed to be locally described by the rigid-body kinematics:

$$\boldsymbol{\psi^n}|_{\boldsymbol{x}} = \boldsymbol{\psi}^n_t|_{g_i} + \boldsymbol{\psi}^n_r|_{g_i} \times \boldsymbol{\zeta} \tag{A.20}$$

where $\boldsymbol{\psi}^n_t|_{g_i}$ and $\boldsymbol{\psi}^n_r|_{g_i}$ are, respectively, the displacement and the rotation associated with the n-th eigenmode of the structure at the centre of mass of the i-th subvolume. For the sake of brevity, we neglect the g_i subscript in the following.

By following the approach presented, it is possible to obtain the following discretised terms:

- centrifugal terms:

$$\begin{aligned} \mathrm{K}^c_{nm} \approx -\boldsymbol{\Omega} \cdot \sum_{i=1}^{N} \frac{1}{2} \{ & m_i \left[2 \left(\boldsymbol{\psi}^n_t \cdot \boldsymbol{\psi}^m_t\right) \mathbf{I} - \boldsymbol{\psi}^n_t \otimes \boldsymbol{\psi}^m_t - \boldsymbol{\psi}^m_t \otimes \boldsymbol{\psi}^n_t\right] + \\ & -2 \left[\mathcal{A}_n : \left(\mathcal{A}_m \, \mathbf{J}^{\boldsymbol{\delta}}_{\boldsymbol{g_i}}\right)\right] \mathbf{I} - \mathcal{A}_n \, \mathbf{J}^{\boldsymbol{\delta}}_{\boldsymbol{g_i}} \, \mathcal{A}_m - \mathcal{A}_m \, \mathbf{J}^{\boldsymbol{\delta}}_{\boldsymbol{g_i}} \, \mathcal{A}_n \} \, \boldsymbol{\Omega} \end{aligned} \tag{A.21}$$

$$\begin{aligned} e^c_n \approx \boldsymbol{\Omega} \cdot \sum_{i=1}^{N} \frac{1}{2} \{ & m_i \left[2 \left(\boldsymbol{R}_{g_i} \cdot \boldsymbol{\psi}^n_t\right) \mathbf{I} - \boldsymbol{R}_{g_i} \otimes \boldsymbol{\psi}^n_t - \boldsymbol{\psi}^n_t \otimes \boldsymbol{R}_{g_i}\right] + \\ & + \mathcal{A}_n \, \mathbf{J}^{\boldsymbol{\delta}}_{\boldsymbol{g_i}} - \mathbf{J}^{\boldsymbol{\delta}}_{\boldsymbol{g_i}} \, \mathcal{A}_n \} \, \boldsymbol{\Omega} \end{aligned} \tag{A.22}$$

- Euler terms:

$$\mathrm{K}_{nm}^{Eu} \approx -\dot{\mathbf{\Omega}} \cdot \sum_{i=1}^{N} \left[m_i \, \boldsymbol{\psi}_t^n \times \boldsymbol{\psi}_t^m - \mathbf{J}_{\boldsymbol{g_i}}^{\boldsymbol{\delta}} \left(\boldsymbol{\psi}_r^n \times \boldsymbol{\psi}_r^m \right) \right] \tag{A.23}$$

$$e_n^{Eu} \approx -\dot{\mathbf{\Omega}} \cdot \sum_{i=1}^{N} \left[m_i \boldsymbol{R}_{g_i} \times \boldsymbol{\psi}_t^n \right] \tag{A.24}$$

- Coriolis terms:

$$\mathrm{D}_{nm}^{Co} \approx -2 \, \mathbf{\Omega} \cdot \sum_{i=1}^{N} \left[m_i \, \boldsymbol{\psi}_t^n \times \boldsymbol{\psi}_t^m - \mathbf{J}_{\boldsymbol{g_i}}^{\boldsymbol{\delta}} \left(\boldsymbol{\psi}_r^n \times \boldsymbol{\psi}_r^m \right) \right] \tag{A.25}$$

where $\mathcal{A}_m$ and $\mathcal{A}_n$ are the skew-symmetric operators associated with the local rotation $\boldsymbol{\psi}_r^m$ and $\boldsymbol{\psi}_r^n$.

References

[1] J. Winters, Z. Saunders, The largest wind turbine ever, Mech. Eng. Mag. 140 (12) (2018) 31–31, `https://doi.org/10.1115/1.2018-DEC-2`.

[2] M. H. Hansen, Aeroelastic instability problems for wind turbines, Wind Energy 10 (6) (2007) 551–577, `https://doi.org/10.1002/we.242`.

[3] L. Gao, S. Yang, A. Abraham, J. Hong, Effects of inflow turbulence on structural response of wind turbine blades, J. Wind Eng. Ind. Aerodyn. 199 (2020) 104–137, `https://doi.org/10.1016/j.jweia.2020.104137`.

[4] NREL, Openfast, `https://github.com/OpenFAST/openfast`, (accessed: October 30, 2020) (2020).

[5] D. H. Hodges, Nonlinear composite beam theory, AIAA, 2006, `https://doi.org/10.2514/4.866821`.

[6] A. T. Patera, A spectral element method for fluid dynamics: laminar flow in a channel expansion, J. Comput. Phys. 54 (3) (1984) 468–488, `https://doi.org/10.1016/0021-9991(84)90128-1`.

[7] T. J. Larsen, A. M. Hansen, How 2 HAWC2, the user's manual, Tech. Rep. Risø-R-1597, Risø National Laboratory, Technical University of Denmark, Roskilde and Kgs. Lyngby, Denmark, https://www.hawc2.dk (2007).

[8] D. Simms, S. Schreck, M. Hand, L. J. Fingersh, NREL unsteady aerodynamics experiment in the NASA-Ames wind tunnel: a comparison of predictions to measurements, Tech. Rep. NREL/TP-500-29494, NREL, Golden, CO (USA), https://doi.org/10.2172/783409 (2001).

[9] J. G. Leishman, Challenges in modelling the unsteady aerodynamics of wind turbines, Wind Energy 5 (2-3) (2002) 85–132, https://doi.org/10.1002/we.62.

[10] S. Gupta, Development of a time-accurate viscous Lagrangian vortex wake model for wind turbine applications, Ph.D. thesis, University of Maryland, College Park, Maryland (2006).

[11] K. M. Kecskemety, J. J. McNamara, Influence of wake dynamics on the performance and aeroelasticity of wind turbines, Renew. Energy 88 (2016) 333–345, https://doi.org/10.1016/j.renene.2015.11.031.

[12] J. F. Manwell, J. G. McGowan, A. L. Rogers, Wind energy explained: theory, design and application, John Wiley & Sons (Chichester, UK), 2010, https://doi.org/10.1002/9781119994367.

[13] G. Van Kuik, J. Peinke, R. Nijssen, D. Lekou, J. Mann, J. N. Sørensen, C. Ferreira, J. van Wingerden, D. Schlipf, P. Gebraad, Long-term research challenges in wind energy – A research agenda by the European Academy of Wind Energy, Wind Energy Sci. 1 (1) (2016) 1–39, https://doi.org/10.5194/wes-1-1-2016.

[14] M. O. L. Hansen, J. N. Sørensen, S. Voutsinas, N. Sørensen, H. A. Madsen, State of the art in wind turbine aerodynamics and aeroelasticity, Prog. Aerosp. Sci. 42 (4) (2006) 285–330, https://doi.org/10.1016/j.paerosci.2006.10.002.

[15] P. Zhang, S. Huang, Review of aeroelasticity for wind turbine: Current status, research focus and future perspectives, Front. Energy 5 (4) (2011) 419–434, https://doi.org/10.1007/s11708-011-0166-6.

[16] G. Cortina, M. Calaf, R. B. Cal, Distribution of mean kinetic energy around an isolated wind turbine and a characteristic wind turbine of a very large wind farm, Phys. Rev. Fluids 1 (7) (2016) 074402, https://doi.org/10.1103/PhysRevFluids.1.074402.

[17] C. Meneveau, Big wind power: Seven questions for turbulence research, J. Turbul. 20 (1) (2019) 2–20, https://doi.org/10.1080/14685248.2019.1584664.

[18] P. R. Spalart, Comments on the feasibility of LES for wings, and on a hybrid RANS/LES approach, in: Proc. of first AFOSR Int. Conf. on DNS/LES , Greyden Press, 1997.

[19] R. Mikkelsen, et al., Actuator disc methods applied to wind turbines, Ph.D. thesis, Technical University of Denmark, Kgs. Lyngby, Denmark (2003).

[20] J. N. Sørensen, W. Z. Shen, Numerical modeling of wind turbine wakes, J. Fluids Eng. 124 (2) (2002) 393–399, https://doi.org/10.1115/1.1471361.

[21] W. Z. Shen, W. J. Zhu, J. N. Sørensen, Actuator line/navier–stokes computations for the mexico rotor: comparison with detailed measurements, Wind Energy 15 (5) (2012) 811–825, https://doi.org/10.1002/we.510.

[22] J. N. Sørensen, R. F. Mikkelsen, D. S. Henningson, S. Ivanell, S. Sarmast, S. J. Andersen, Simulation of wind turbine wakes using the actuator line technique, Philos. T. R. Soc. A 373 (2035) (2015) 20140071, https://doi.org/10.1098/rsta.2014.0071.

[23] S. Xie, C. L. Archer, Self-similarity and turbulence characteristics of wind turbine wakes via large-eddy simulation, Wind Energy 18 (10) (2015) 1815–1838, https://doi.org/10.1002/we.1792.

[24] M.-C. Hsu, Y. Bazilevs, Fluid–structure interaction modeling of wind turbines: simulating the full machine, Comput. Mech. 50 (6) (2012) 821–833, https://doi.org/10.1007/s00466-012-0772-0.

[25] J. Jonkman, S. Butterfield, W. Musial, G. Scott, Definition of a 5-MW reference wind turbine for offshore system development, Tech. Rep. NREL/TP-500-38060, NREL, Golden, CO (USA), https://doi.org/10.2172/947422 (2009).

[26] J. C. Heinz, Partitioned fluid-structure interaction for full rotor computations using CFD, Ph.D. thesis, Technical University of Denmark, Kgs. Lyngby, Denmark (2013).

[27] J. A. Michelsen, Block structured Multigrid solution of 2D and 3D elliptic PDE's, Technical University of Denmark, 1994.

[28] D. O. Yu, O. J. Kwon, Predicting wind turbine blade loads and aeroelastic response using a coupled CFD–CSD method, Renew. Energy 70 (2014) 184–196, https://doi.org/10.1016/j.renene.2014.03.033.

[29] M.-S. Jeong, M.-C. Cha, S.-W. Kim, I. Lee, T. Kim, Effects of torsional degree of freedom, geometric nonlinearity, and gravity on aeroelastic behavior of large-scale horizontal axis wind turbine blades under varying wind speed conditions, J. Renew. Sustain. Energy 6 (2) (2014) 023126, https://doi.org/10.1063/1.4873130.

[30] Z. Li, B. Wen, X. Dong, Z. Peng, Y. Qu, W. Zhang, Aerodynamic and aeroelastic characteristics of flexible wind turbine blades under periodic unsteady inflows, J. Wind Eng. Ind. Aerodyn. 197 (2020) 104057, https://doi.org/10.1016/j.jweia.2019.104057.

[31] B. Dose, H. Rahimi, I. Herráez, B. Stoevesandt, J. Peinke, Fluid-structure coupled computations of the NREL 5 MW wind turbine by means of CFD, Renew. Energy 129 (2018) 591–605, https://doi.org/10.1016/j.renene.2018.05.064.

[32] H. Jasak, A. Jemcov, Z. Tukovic, et al., OpenFOAM: A C++ library for complex physics simulations, in: Int. workshop on coupled methods in numerical dynamics, IUC Dubrovnik Croatia, 2007.

[33] E. Reissner, On one-dimensional finite-strain beam theory: the plane problem, Zeitschrift für angewandte Mathematik und Physik ZAMP 23 (5) (1972) 795–804, `https://doi.org/10.1007/BF01602645`.

[34] M. Sprague, S. Ananthan, G. Vijayakumar, M. Robinson, ExaWind: A multi-fidelity modeling and simulation environment for wind energy, in: J. Phys. Conf. Series, 2020.

[35] S. Domino, Sierra low mach module: Nalu theory manual 1.0, Tech. Rep. SAND2015-3107W, Sandia National Laboratories (2015).

[36] C. Farhat, M. Lesoinne, On the accuracy, stability, and performance of the solution of three-dimensional nonlinear transient aeroelastic problems by partitioned procedures, in: 37th Structure, Structural Dynamics and Materials Conf., 1996, `https://doi.org/10.2514/6.1996-1388`.

[37] Y. Li, A. Castro, T. Sinokrot, W. Prescott, P. Carrica, Coupled multi-body dynamics and CFD for wind turbine simulation including explicit wind turbulence, Renew. Energy 76 (2015) 338–361, `https://doi.org/10.1016/j.renene.2014.11.014`.

[38] J. Mann, Wind field simulation, Probabilistic Eng. Mech. 13 (4) (1998) 269–282, `https://doi.org/10.1016/S0266-8920(97)00036-2`.

[39] R. Storey, S. Norris, K. Stol, J. Cater, Large eddy simulation of dynamically controlled wind turbines in an offshore environment, Wind Energy 16 (6) (2013) 845–864, `https://doi.org/10.1002/we.1525`.

[40] J. M. Jonkman, M. L. Buhl Jr, Fast user's guide-updated august 2005, Tech. rep., NREL, Golden, CO (USA) (2005).

[41] R. Storey, S. Norris, J. Cater, An actuator sector method for efficient transient wind turbine simulation, Wind Energy 18 (4) (2015) 699–711, https://doi.org/10.1002/we.1722.

[42] M. J. Churchfield, S. Lee, J. Michalakes, P. J. Moriarty, A numerical study of the effects of atmospheric and wake turbulence on wind turbine dynamics, J. Turbul. (13) (2012) N14, https://doi.org/10.1080/14685248.2012.668191.

[43] S. Lee, M. Churchfield, P. Moriarty, J. Jonkman, J. Michalakes, A numerical study of atmospheric and wake turbulence impacts on wind turbine fatigue loadings, J. Sol. Energy Eng. 135 (3), https://doi.org/10.1115/1.4023319.

[44] H. Meng, F.-S. Lien, L. Li, Elastic actuator line modelling for wake-induced fatigue analysis of horizontal axis wind turbine blade, Renew. Energy 116 (2018) 423–437, https://doi.org/10.1016/j.renene.2017.08.074.

[45] H. Meng, F.-S. Lien, G. Glinka, L. Li, J. Zhang, Study on wake-induced fatigue on wind turbine blade based on elastic actuator line model and two-dimensional finite element model, Wind Eng. 43 (1) (2019) 64–82, https://doi.org/10.1177/0309524X18819898.

[46] P. Orlandi, S. Leonardi, DNS of turbulent channel flows with two-and three-dimensional roughness, J. Turbul. (7) (2006) N73, https://doi.org/10.1080/14685240600827526.

[47] C. Santoni, E. J. García-Cartagena, U. Ciri, L. Zhan, G. Valerio Iungo, S. Leonardi, One-way mesoscale-microscale coupling for simulating a wind farm in North Texas: Assessment against SCADA and LiDAR data, Wind Energy 23 (3) (2020) 691–710, https://doi.org/10.1002/we.2452.

[48] J. Smagorinsky, General circulation experiments with the primitive equations: I. The basic experiment, MWR 91 (3) (1963) 99–164, https://doi.org/10.1175/1520-0493(1963)091%3C0099:GCEWTP%3E2.3.CO;2.

[49] U. Ciri, G. Petrolo, M. V. Salvetti, S. Leonardi, Large-eddy simulations of two in-line turbines in a wind tunnel with different inflow conditions, Energies 10 (6) (2017) 821, https://doi.org/10.3390/en10060821.

[50] U. Ciri, M. A. Rotea, S. Leonardi, Effect of the turbine scale on yaw control, Wind Energy 21 (12) (2018) 1395–1405, https://doi.org/10.1002/we.2262.

[51] P. Orlandi, Fluid flow phenomena: a numerical toolkit, Vol. 55, Springer Science & Business Media, 2012, https://doi.org/10.1023/A:1010397420189.

[52] W. Z. Shen, J. N. Sørensen, R. Mikkelsen, Tip loss correction for actuator/Navier–Stokes computations, J. Sol. Energy Eng. 127 (2) (2005) 209–213, https://doi.org/10.1115/1.1850488.

[53] N. Troldborg, J. Sørensen, R. Mikkelsen, Actuator line modeling of wind turbine wakes, Ph.D. thesis, Technical University of Denmark, Kgs. Lyngby, Denmark (2009).

[54] P. K. Jha, M. J. Churchfield, P. J. Moriarty, S. Schmitz, Guidelines for volume force distributions within actuator line modeling of wind turbines on large-eddy simulation-type grids, J. Sol. Energy Eng. 136 (3), https://doi.org/10.1115/1.4026252.

[55] M. J. Churchfield, S. J. Schreck, L. A. Martinez, C. Meneveau, P. R. Spalart, An advanced actuator line method for wind energy applications and beyond, in: 35th Wind Energy Symp., 2017, https://doi.org/10.2514/6.2017-1998.

[56] L. A. Martínez-Tossas, M. J. Churchfield, C. Meneveau, Optimal smoothing length scale for actuator line models of wind turbine blades based on gaussian body force distribution, Wind Energy 20 (6) (2017) 1083–1096, https://doi.org/10.1002/we.2081.

[57] C. Santoni, K. Carrasquillo, I. Arenas-Navarro, S. Leonardi, Effect of tower and nacelle on the flow past a wind turbine, Wind Energy 20 (12) (2017) 1927–1939, https://doi.org/10.1002/we.2130.

[58] K. E. Johnson, L. Y. Pao, M. J. Balas, L. J. Fingersh, Control of variable-speed wind turbines: standard and adaptive techniques for maximizing energy capture, IEEE Control Syst. Mag. 26 (3) (2006) 70–81, https://doi.org/10.1109/MCS.2006.1636311.

[59] M. Hansen, Improved modal dynamics of wind turbines to avoid stall-induced vibrations, Wind Energy 6 (2) (2003) 179–195, https://doi.org/10.1002/we.79.

[60] C. Reschke, Flight loads analysis with inertially coupled equations of motion, in: AIAA Atmospheric Flight Mechanics Conference and Exhibit, 2005, https://doi.org/10.2514/6.2005-6026.

[61] F. Saltari, C. Riso, G. D. Matteis, F. Mastroddi, Finite-element-based modeling for flight dynamics and aeroelasticity of flexible aircraft, J. Aircr. 54 (6) (2017) 2350–2366, https://doi.org/10.2514/1.C034159.

[62] J. S. Przemieniecki, Theory of matrix structural analysis, Courier Corporation, 1985, https://doi.org/10.1016/0022-460X(69)90212-0.

[63] J. Chung, G. Hulbert, A time integration algorithm for structural dynamics with improved numerical dissipation: the generalized-α method, J. Appl. Mech.https://doi.org/10.1115/1.2900803.

[64] E. R. Van Driest, On turbulent flow near a wall, J. Aeronaut. Sci. 23 (11) (1956) 1007–1011, https://doi.org/10.2514/8.3713.

[65] J. Feliciano, G. Cortina, A. Spear, M. Calaf, Generalized analytical displacement model for wind turbine towers under aerodynamic loading, J. Wind. Eng. Ind. Aerodyn. 176 (2018) 120–130, https://doi.org/10.1016/j.jweia.2018.03.018.

[66] H. J. Sutherland, On the fatigue analysis of wind turbines, Tech. rep., Sandia National Labs, Albuquerque, NM (US), https://doi.org/10.2172/9460 (1999).

[67] M. L. Buhl, MCrunch user's guide for version 1.00, Tech. Rep. NREL/TP-500-43139, NREL, Golden, CO (USA) (2008).

[68] S. D. Downing, D. Socie, Simple rainflow counting algorithms, Int. J. Fatigue 4 (1) (1982) 31–40, https://doi.org/10.1016/0142-1123(82)90018-4.

[69] M. Miner, Cumulative fatigue damage, J. Appl. Mech. 12 (3) (1945) 159–164.

[70] Y. Dubief, F. Delcayre, On coherent-vortex identification in turbulence, J. Turbul. 1 (1) (2000) 011–011, https://doi.org/10.1088/1468-5248/1/1/011.

[71] L. P. Chamorro, S.-J. Lee, D. Olsen, C. Milliren, J. Marr, R. Arndt, F. Sotiropoulos, Turbulence effects on a full-scale 2.5 MW horizontal-axis wind turbine under neutrally stratified conditions, Wind Energy 18 (2) (2015) 339–349, https://doi.org/10.1002/we.1700.

[72] K. Howard, J. Hu, L. Chamorro, M. Guala, Characterizing the response of a wind turbine model under complex inflow conditions, Wind Energy 18 (4) (2015) 729–743, https://doi.org/10.1002/we.1724.

[73] M. Calaf, C. Meneveau, J. Meyers, Large eddy simulation study of fully developed wind-turbine array boundary layers, Phys. Fluids 22 (1) (2010) 015110, https://doi.org/10.1063/1.3291077.

[74] C. L. Archer, S. Mirzaeisefat, S. Lee, Quantifying the sensitivity of wind farm performance to array layout options using large-eddy simulation, Geophys. Res. Lett. 40 (18) (2013) 4963–4970, https://doi.org/10.1002/grl.50911.

[75] M. Melius, R. B. Cal, K. Mulleners, Dynamic stall of an experimental wind turbine blade, Phys. Fluids 28 (3) (2016) 034103, https://doi.org/10.1063/1.4942001.